Development and assessment of modelling strategies to predict failure in tow-based discontinuous composites

Yizhuo Li, Soraia Pimenta*

Department of Mechanical Engineering, Imperial College London, South Kensington Campus, London, SW7 2AZ

Abstract

Tow-based discontinuous composites (TBDCs) are a growing class of materials that combine manufacturability, light-weight, and high performance. This study proposes multi-scale modelling approaches to predict the tensile strength and failure envelopes of tow-based discontinuous composites, by representing the actual composite (with randomly-oriented tows) as an equivalent ply-by-ply laminate. Several modelling approaches are considered for the different scales, including (i) a stochastic bi-linear shear-lag formulation accounting for the random location of tow-ends and matrix cracking, (ii) a novel failure criterion for a discontinuous uni-directional ply accounting for the interaction between tow pull-out and transverse failure, and (iii) a ply-discount method or a maximum strain energy criterion for the final failure of the composite. The model computes full failure envelopes for ply-by-ply laminates equivalent to TBDCs within minutes, and the results show good agreement with experimental data.

Keywords: `Discontinuous reinforcement; Strength; Analytical modelling; Multi-scale material.`

1. Introduction

Tow-Based Discontinuous Composites (TBDCs) are a growing class of high-performance materials for high-volume production of structural applications, composed of carbon-fibre tows randomly oriented and distributed in a polymeric matrix. The main advantages of using TBDCs are that (i) the discontinuous nature of the tows allows these materials to be moulded in complex shapes, which significantly improves the manufacturability of TBDCs compared to conventional Continuous-Fibre Composites (CFCs), and (ii) the tow-based architecture of TBDCs allows for a high fibre-content and hence preserves the good mechanical properties of CFCs [1–3].

---

*Corresponding author
Email address:* `soraia.pimenta@imperial.ac.uk` (Soraia Pimenta)

Nomenclature

Uppercase Roman variables

E	Young's modulus
F_I	failure index
G	shear modulus
$\mathcal{G}$	fracture toughness
M	global stress factor
N	numerical parameter
R	aspect ratio
S	shear strength
U	specific strain energy
V	volume fraction
X	longitudinal strength
Y	transverse strength
$\mathbf{Q}$	stiffness matrix
$\mathbf{S}$	compliance matrix

Lowercase Roman variables

d	damage variable
l	length
m	local stress factor
n	number of fibres in a tow
s	standard deviation
t	thickness
$\mathbf{v}$	eigenvector

Abbreviations

CFC	continuous fibre composites
DEA	decomposed energy approach
DFC	discontinuous fibre composites
EL	equivalent laminate
FE	finite element
FPF	first-ply failure
ITS	interacted tension-shear
PDM	ply-discount method
RC	random composite
RVE	representative volume element
SLM	shear-lag model
TBDC	tow-based discontinuous composite
TEA	total energy approach
UD	uni-directional

Lowercase Greek variables

$\bar{\alpha}, \bar{\beta}, \bar{\gamma}$	local proportional loading (see Figure 2c)
γ	shear strain
ε	tensile strain
η	friction coefficient
θ	orientation of a ply
ν	Poisson's ratio
σ	direct stress
τ	shear stress
ϕ	fibre diameter

Superscripts

$*$	ultimate value
∞	far-field
C	compressive
F	fracture
is	in-situ
T	tensile

Subscripts

1,2	local ply coordinates
II	mode II fracture
char	characteristic
crit	critical
D	discontinuous
dev	deviatoric component
f	fibre
g	global
l	local
m	matrix/interface
mean	mean value
o	overlap
SL	shear-lag
t	tow
vol	volumetric component
x, y	global coordinates

Uppercase Greek variables

$\bar{A}, \bar{B}, \bar{\Gamma}$	global proportional loading (see Figure 2a)

Operators

$\hat{}$	normalised unit vector

This combination of manufacturability and good mechanical properties makes TBDCs appealing for high-volume production of structural applications. Some of the commercial applications of TBDCs include window frames of the 787 Dreamliner [4], the inner monocoque and suspension control arm of the 'Sesto Elemento' concept car from Automobili Lamborghini [5], and the Diablo Octane drivers from Callaway Golf [6].

In the literature, mechanical properties of TBDCs with different tow geometries and resin types have been measured. It has been found that the modulus of TBDCs generally falls between 40 and 50 GPa, whereas the tensile strength lies between 250 and 500 MPa [1, 2, 7, 8]. In most studies, it has also been shown that, unlike conventional continuous-fibre composites, TBDCs have a slightly lower strength under tension than under compression [2, 9].

Accurate yet computationally efficient models are required to optimise the microstructure of TBDCs and to design lightweight structures. However, the mechanical response of TBDCs is difficult to predict due to their complicated architecture: discontinuous and randomly oriented tows create complex stress fields at the tow ends, and lead to a combined failure mode of tow fracture and tow pull-out [3]. Some of these challenges are also shared by conventional Discontinuous Fibre Composites (DFCs), with dispersed fibres rather than tows, for which several models are available in the literature [1, 10–15].

To account for the randomly-oriented architecture of fibres and tows, an equivalent laminate analogy has been widely adopted for DFCs in general [11, 12], and for TBDCs in particular [1, 16]. This analogy structures the random orientations of the tows into individual Uni-Directional (UD) plies (each ply containing fibres/tows aligned in a given direction), which are then stacked to form a ply-by-ply laminate with ply-orientation distribution equivalent to that of the randomly-oriented composite. It has been shown experimentally [7] that the equivalent laminate analogy is able to capture the failure mechanisms of TBDCs, although that study also highlighted the need to consider the intrinsic variability of the microstructure in TBDCs (which is not present in their equivalent laminates in order to predict their strength) [7].

Deformation and failure of an equivalent ply-by-ply discontinuous laminate are commonly predicted through the homogenisation of the second and forth order stiffness and strength tensors, assuming iso-strains [1, 10, 11]; although this method provides reasonable predictions for elastic properties, it lacks the ability to capture the behaviour of the equivalent laminate beyond the elastic region [10]. Alternatively, the strength of laminates can be predicted through a first-ply-failure analysis; this method usually underestimates the strength of CFCs [17], but it has produced reasonable estimates for TBDCs [16]. The most successful methods for predicting the strength of CFCs use a progressive failure analysis, where the stiffness of damaged plies is progressively reduced throughout the simulation [18].

Using the equivalent laminate analogy to model DFCs requires defining failure criteria not only

3

for the overall laminate (as described above), but also for the individual plies at different orientations.

Phenomenological failure criteria (e.g. Tsai-Wu [19] and Tsai-Hill [20]) are simple to implement, but are not physically-based and cannot predict the failure mechanisms [19]. Physically-based failure criteria for UD CFCs often predict tensile fibre failure and tensile/shear matrix failure independently, and assume no interaction between the two [21–23]; while this is a reasonable assumption for *continuous composites*, it neglects the interaction between longitudinal (fibre-dominated) and transverse (matrix-dominated) loading during fibre/tow pull-out in *discontinuous composites*. Some failure criteria also take into account in-situ effects for the strength of embedded plies in a laminate, thus predicting a strength reduction with increasing ply thickness [22].

To account for the presence of discontinuities in the reinforcement of DFCs or TBDCs, shear-lag models are one of the most widely adopted strategies in the literature [1, 11, 14, 15]. Traditionally, it has been assumed that the matrix is perfectly-plastic as proposed by Kelly and Tyson [14], which assumes that the failure mechanisms of a discontinuous UD composite are either (i) matrix yielding in shear and pull-out of short (or small aspect-ratio) reinforcing units, and (ii) longitudinal tensile fracture of long (or large aspect-ratio) reinforcing units. Kelly-Tyson's perfect-plastic model [14] predicts an increase in the strength of discontinuous composites as the aspect-ratio of reinforcing units increases (up to the critical aspect-ratio), but predicts no effect due to changes in the absolute dimensions of the reinforcement if the aspect-ratio remains constant. Pimenta and Robinson [15] developed a non-linear shear-lag model which considers matrix/interfacial failure and more generic matrix constitutive laws, and concluded that brittle matrix/interfacial cracking — governed by the finite fracture toughness of the matrix/interface rather than by its strength — is the dominating failure mechanism for discontinuous composites with long and thick reinforcing units (which is the case for TBDCs).

Most shear-lag models [1, 11, 14, 15] assume a constant length for the stress transfer between reinforcing units. However, Henry and Pimenta [24] demonstrated that this assumption can lead to a significant overprediction of the ultimate strength of a discontinuous composite, and proposed a stochastic shear-lag model which accounts for the random location of fibre-ends. Applying this concept to TBDCs by considering the randomness in tow-end locations would allow one to capture the combination of failure modes (tow pull-out and tow fracture) that occurs in these materials; it would also contribute to capture the highly heterogeneous nature of TBDCs, which has been shown to lead to a large variability in local strains [25], and which may significantly affect the location of the critical point and the final failure load in a structure [26].

Some authors further developed the modelling strategies mentioned above in order to predict failure of TBDCs. Harper [1] developed a multi-scale strength model for TBDCs, based on the properties

and geometry of the tows, and Kelly-Tyson's perfectly-plastic shear-lag thoery [14]. Feraboli et al. [16] modelled TBDCs as $[0°/90°/+45°/-45°]_s$ laminates with continuous plies, and observed experimentally that the strength of TBDCs coincide with the failure of the $90°$ ply (first ply failure) in the equivalent laminate. These models provide first estimates for the strength of TBDCs, but they cannot account for some features observed experimentally (as, for instance, the significant decrease in the strength of TBDCs with increased tow thickness [7]).

Selezneva et al. [27] modelled the strength of TBDCs by considering a stochastic 2D Representative Volume Element (RVE) with randomly-oriented tows, and calculating the strength of the RVE considering a simplified version of Pimenta and Robinson's shear-lag model [15]. This model [27] predicts the strength and crack propagation path in TBDCs under uni-axial tensile load, but it considers only 2D sections of the composite and cannot calculate failure envelopes under more complicated loading conditions.

In addition to the analytical models described above, numerical models for TBDCs have also been developed [28, 29]. These models consider either an explicit representation of the fibres/tows [29], or a discrete grid of equivalent laminates with stochastic layups [28], and use Finite Element (FE) simulations of RVEs to cope with the variability in microstructures and the complexity of stress fields. Consequently, these numerical/FE models are computationally very expensive.

Overall, there is a striking lack of computationally efficient models to predict the strength of TBDCs, while accounting for the specificities of these materials. Therefore, this study proposes modelling strategies to predict the strength and failure envelopes of TBDCs, and to assess the effect of several simplifications commonly used in the literature. The model (described in Section 2) idealises the architecture of the randomly-oriented discontinuous composite as an equivalent ply-by-ply laminate, and the mechanical response is built up from the tow to the laminate scale, taking into account (i) the finite toughness of the matrix or tow interface, (ii) the random location of tow-ends, (iii) the interaction between tow pull-out and matrix failure, and (iv) the final failure of the laminate under a generic plane-stress state. Model results are presented and compared to experiments in Section 3, and they are further discussed in Section 4. The main conclusions of this study are presented in Section 5.

2. Model development

2.1. Multi-scale framework

Consider the TBDC plate represented in Figure 1. The material consists of a network of randomly-oriented discontinuous tows embedded in a polymeric matrix. All tows are geometrically identical, and they are the smallest reinforcing unit considered in this study. The tows are characterised by the following properties (which are used as inputs for the model):

5

- Geometry: tow length (l_t), tow width (w_t), and tow thickness (t_t) (the tow width and thickness can be measured directly in chip- or prepreg-based TBDCs, or estimated from the tow-filament-count and the fibre volume fraction in SMC-based TBDCs).

- In-plane elastic constants: tensile moduli (E_1, E_2), shear moduli (G_{12}), and Poisson's ratio (ν_{12});

- In-plane strengths: tensile (superscript $^\mathrm{T}$) strength in the longitudinal direction (X^T), and tensile and compressive (superscript $^\mathrm{C}$) strengths in the transverse direction $(Y^\mathrm{T}$ and $Y^\mathrm{C})$, and in-plane shear strength (S);

- Fracture toughness for an interfacial crack propagating around or along the tows (i.e. without breaking fibres) in mode II $(\mathcal{G}_{\mathrm{IIc}})$;

These mechanical properties of the tows can be taken as the properties of the equivalent UD continuous composite, consisting of the same fibre-matrix system and the same fibre volume fraction.

The TBDC material is assumed to be under plane-stress (which is suitable for thin components), so that the remote loading vector can be defined as

$$\boldsymbol{\sigma}_\mathrm{g} = [\sigma_x, \sigma_y, \tau_{xy}]^\mathrm{T} = M \cdot \widehat{\boldsymbol{\sigma}}_\mathrm{g}, \quad \text{with} \quad \widehat{\boldsymbol{\sigma}}_\mathrm{g} = [\bar{A}, \bar{B}, \bar{\Gamma}]^\mathrm{T} : \sqrt{\bar{A}^2 + \bar{B}^2 + \bar{\Gamma}^2} = 1, \tag{1}$$

where $\widehat{\boldsymbol{\sigma}}_\mathrm{g}$ defines a unit loading vector and M defines the magnitude of the applied load. Since the tensile strength of TBDCs is lower than their compressive strength, this work will focus on tensile-dominated loading cases, with $\sigma_x > 0$ and $\sigma_y > 0$; in this case, even if locally compressive stresses arise due to Poisson's effects, they will not be sufficient to lead to compressive failure of tows, and, therefore, the longitudinal compressive strength of the tows is needed as a model input. In contrast, the transverse compressive strength of the tows is required as an input parameter, because it will be used to formulate the failure criterion in Eq. 6, Section 2.3.2.

In order to deal with the complicated architecture of TBDCs, a multi-scale approach based on an equivalent ply-by-ply laminate (Figure 2) is adopted [1, 11]. This approach decouples the effect of the discontinuous nature of the tows from the effect of the random tow orientations. The model is implemented as shown in Figure 3, where each scale is explained in Section 2.2 to Section 2.4, building up from the micro-scale (i.e. tow) to the macro-scale (i.e. laminate).

2.2. Tensile strength of a discontinuous UD ply (micro-scale)

The discontinuous reinforcement in the UD plies in the equivalent laminate (Figure 2c) results in a decrease in the longitudinal tensile strength when compared to a continuous ply. This is because the presence of tow ends reduces the tow stresses near the ends of the tow, and generates shear stresses in the matrix and at the tow interface, which leads to an extra failure mode of tow pull-out. The micro-scale model developed in this section aims to calculate the longitudinal tensile strength of a discontinuous UD ply $(X_\mathrm{D}^\mathrm{T})$, based on a shear-lag stress transfer at the interface between the tows.

It has been experimentally observed [7] that, although TBDCs have some resin-rich packets, they do not present a significant resin-rich layer between the tows. Therefore, we assume that the thickness of the shear-lag interface is equal to the inter-fibre distance in the composite, which is calculated assuming a square fibre packing:

$$t_{\mathrm{m}} = \left(\sqrt{\frac{\pi}{4V_{\mathrm{f}}}} - 1 \right) \cdot \phi_{\mathrm{f}}, \tag{2}$$

where ϕ_{f} is fibre diameter and V_{f} is fibre volume fraction of the TBDC material. We have verified that this assumption does not significantly effect the strength predicted for TBDCs (for instance, an increase of 50% on the thickness of the interface results in less than a 0.3% difference in the tensile strengths predicted for representative inputs, as those used for Figure 9).

The shear-lag model proposed here is based on Pimenta and Robinson's non-linear shear-lag model for perfectly-staggered brick-and-mortar composites [15] (which considers the effect of both plastic yielding and brittle fracture of the brick interfaces) and its stochastic extension by Henry and Pimenta [24] (which predicts the mechanical response of a discontinuous UD ply with randomly located fibre-ends). In the present paper, these models [15, 24] are modified by replacing the individual bricks or fibres with tows, and the matrix with a thin tow-to-tow interface (of thickness t_{m}), as shown in Figure 4.

The tows are considered to be arranged in a UD ply with the 3D geometry schematically shown in Figure 4. It is assumed that the shear-lag stresses are transferred to a tow from its four nearest neighbours; the stress-transfer occurs along the perimeter (given by $2 \cdot (w_{\mathrm{t}} + t_{\mathrm{t}})$) of the cross-section of each tow, and builds up tensile stresses within the area (given by $w_{\mathrm{t}} \cdot t_{\mathrm{t}}$) of the cross-section of the tow. Therefore, the *equivalent characteristic thickness* for the shear-lag model [15] is defined as $t_{\mathrm{char}} = w_{\mathrm{t}} \cdot t_{\mathrm{t}}/[2 \cdot (w_{\mathrm{t}} + t_{\mathrm{t}})]$; this definition of the characteristic thickness effectively reduces the 3D problem shown in Figure 4a to a 1D problem, regardless of the relative position of the tows, and regardless of the tow surface at which shear-stresses are transmitted.

These considerations allow the original models [15, 24] to be simplified, since the strength of the tows can be assumed to be deterministic (due to the large number of fibres in each tow (typically between 3k and 15k), which should lead to a much lower coefficient of variation in the strength to a tow compared to that of an individual fibre [30]), and the generic constitutive law of the tow interface can be assumed to be bi-linear (defined by the shear modulus G_{12}, shear strength S, and mode-II fracture toughness $\mathcal{G}_{\mathrm{IIc}}$). This leads to a 4-steps approach to calculate the strength of a UD TBDC ply with randomly located tow-ends (see Figure 4):

1. Assume a square arrangement of the tows, so that each tow interacts with its four nearest neighbours (see Figure 4). Calculate the stress-strain response $\sigma_{\mathrm{o}}(\varepsilon_{\mathrm{o}}; l_{\mathrm{o}}, t_{\mathrm{o}})$ of each *overlap* (sub-

7

script $_o$) defined between the ends of two neighbouring tows, which depends on the random tow overlap length $l_o \in [0, l_t]$ and random tow overlap thickness $t_o \in [0, 2t_{\text{char}}]$. The overlap stress-strain response is calculated based on a simplification of Pimenta and Robinson's [15] shear-lag model with a bi-linear constitutive law, as detailed in Appendix A. Representative resulting stress-strain responses of the overlaps are illustrated in Figure 5b; to improve computational efficiency, the stress-strain response of overlap is calculated at N_{lo} and N_{to} discrete values of the overlap length and overlap thickness only.

2. Calculate the stress-strain response $\sigma_i(\varepsilon_i; l_o, t_o)$ of an *interaction* (subscript $_i$) between two neighbouring tows, consisting of a series of two overlaps of lengths l_o and $l_t - l_o$, and overlap thickness t_o. The strain of the interaction is calculated as $\varepsilon_i(\sigma_i; l_o, t_o) = [\varepsilon_o(\sigma_i; l_o, t_o) \cdot l_o + \varepsilon_o(\sigma_i; l_t - l_o, t_o) \cdot (l_t - l_o)]/l_t$ up to interfacial failure of the weakest overlap, after which $\sigma_i = 0$ for any applied strain ε_i.

3. Model the stress-strain response of a single *tow* (subscript $_t$), considering that its stress σ_t is built up through the interactions with the four neighbouring tows (characterised by overlapping lengths $l_o = \{l_1, l_2, l_3, l_4\}$ and thicknesses $t_o = \{t_1, t_2, t_3, t_4\}$, where $t_1 + t_2 + t_3 + t_4 = 4 \cdot t_{\text{char}}$, see Figure 4,) in parallel; this is equivalent to considering periodic boundary conditions along the longitudinal direction of the central tows and its four neighbours, without constraining the transverse direction. Imposing a uniform remote strain ε_t to the tow, the stress in a tow can be defined as

$$\sigma_t(\varepsilon_t; l_1, l_2, l_3, l_4, t_1, t_2, t_3, t_4) = \frac{\sigma_i(\varepsilon_t; l_1, t_1) + \sigma_i(\varepsilon_t; l_2, t_2) + \sigma_i(\varepsilon_t; l_3, t_3) + \sigma_i(\varepsilon_t; l_4, t_4)}{4}. \quad (3)$$

The stress in a tow is set to 0 when σ_t exceeds the tow tensile strength X^T at a given strain ε_t.

4. Calculate the stress-strain curve of a *representative volume element (RVE)* containing a sufficiently large number N_{RVE} of parallel tows, by imposing uniform remote strains ε_{RVE} to all tows, so that $\sigma_{\text{RVE}}(\varepsilon_{\text{RVE}}) = \Sigma_{i=1}^{N_{\text{RVE}}} \{\sigma_{t,i}(\varepsilon_{\text{RVE}}; l_{1,i}, l_{2,i}, l_{3,i}, l_{4,i}, t_{1,i}, t_{2,i}, t_{3,i}, t_{4,i})\}/N_{\text{RVE}}$.

The ultimate tensile strength of the discontinuous ply (X_D^T) is given as the peak of this stress-strain curve: $X_D^T = \max(\sigma_{\text{RVE}})$.

Because this model uses the strength and mode-II fracture toughness of the tow interface as inputs, it can be used to assess the effect of considering interfacial failure due to both plastic yielding (governed by the interfacial shear strength S) and brittle cracking (governed by the interfacial fracture toughness $\mathcal{G}_{\text{IIc}}$); by modelling both forms of interfacial failure, the influence of absolute tow dimensions and relative aspect-ratio can be fully explored (see Section 3.2.1). Similarly, by considering individual tow interactions explicitly, this model can be used to assess the effect of assuming perfectly-staggered tows (in which case $l_o = l_t/2$ and $t_o = t_{\text{char}}$), or considering randomness in overlap lengths and thicknesses (see Section 3.2.1).

8

2.3. Failure criterion for a UD discontinuous ply

2.3.1. Stress transformation from global to local coordinates

For each ply with orientation θ in the equivalent laminate (see Figure 2b), the global (subscript g) stress applied $\boldsymbol{\sigma}_{\mathrm{g}} = [\sigma_x, \sigma_y, \tau_{xy}]^{\mathrm{T}} = M \cdot [\bar{A}, \bar{B}, \bar{\Gamma}]^{\mathrm{T}}$ (in global $\{x, y\}$ coordinates) is decomposed and transformed into the local (subscript l) coordinate system $\{1,2\}$, using classical laminate theory and assuming uniform remote strain fields:

$$\boldsymbol{\sigma}_{\mathrm{l}} = \mathbf{Q}_{\mathrm{l}} \cdot \boldsymbol{\varepsilon}_{\mathrm{l}} = \mathbf{Q}_{\mathrm{l}} \cdot (\mathbf{T} \cdot \boldsymbol{\varepsilon}_{\mathrm{g}}) = \mathbf{Q}_{\mathrm{l}} \cdot [\mathbf{T} \cdot (\mathbf{Q}_{\mathrm{g}}^{-1} \cdot \boldsymbol{\sigma}_{\mathrm{g}})], \tag{4}$$

where $\mathbf{Q}_{\mathrm{g}}$ and $\mathbf{Q}_{\mathrm{l}}$ are respectively the global (laminate) and local (UD ply) stiffness matrices, and $\mathbf{T}$ is transformation matrix [19]. The local stress field in each ply can therefore be written using a proportional loading factor m as $\boldsymbol{\sigma}_{\mathrm{l}} = [\sigma_1, \sigma_2, \tau_{12}]^{\mathrm{T}} = m \cdot \widehat{\boldsymbol{\sigma}}_{\mathrm{l}} = m \cdot [\bar{\alpha}, \bar{\beta}, \bar{\gamma}]^{\mathrm{T}}$, where the normalised unit local loading vector $\widehat{\boldsymbol{\sigma}}_{\mathrm{l}}$ is

$$\widehat{\boldsymbol{\sigma}}_{\mathrm{l}} = [\bar{\alpha}, \bar{\beta}, \bar{\gamma}]^{\mathrm{T}} = \mathbf{Q}_{\mathrm{l}} \cdot (\mathbf{T} \cdot \mathbf{Q}_{\mathrm{g}}^{-1} \cdot \widehat{\boldsymbol{\sigma}}_{\mathrm{g}}) = \mathbf{Q}_{\mathrm{l}} \cdot (\mathbf{T} \cdot \mathbf{Q}_{\mathrm{g}}^{-1} \cdot [\bar{A}, \bar{B}, \bar{\Gamma}]^{\mathrm{T}}), \quad \text{and } m \equiv M. \tag{5}$$

The failure criterion described in Section 2.3.2 aims to calculate the local failure factor $m^*(\theta)$ for each ply orientation θ, considering a given global loading unit vector $\widehat{\boldsymbol{\sigma}}_{\mathrm{g}} = [\bar{A}, \bar{B}, \bar{\Gamma}]^{\mathrm{T}}$.

2.3.2. Interactive Tension-Shear (ITS) criterion

Many physically-based failure criteria for CFCs — for instance, Hashin's [21] and LaRC05 [22] failure criteria — consider no interaction between (i) longitudinal-tensile and (ii) transverse-tensile/shear failure modes, as they are dominated respectively by (i) fibre and (ii) matrix/interfacial failure (which are fairly independent from each other in CFCs). However, TBDCs may fail under longitudinal tension by tow pull-out (which is governed by failure of the tow interface, thus also affected by the coupling between shear-lag and transverse loading), and therefore the coupling between longitudinal and transverse failure modes should be considered. To account for this effect, the shear-lag model described in Section 2.2 will be integrated in an interactive tension-shear criterion, in order to obtain the longitudinal-tension vs. in-plane shear failure envelope for a discontinuous UD ply, as described below.

Consider a UD ply in the equivalent laminate with non-zero applied in-plane shear stress $|\tau_{12}| \leq S$; if this is superposed with a longitudinal tensile stress σ_1, the ability of the tow interface to transfer stresses through shear-lag is now reduced to $S_{\mathrm{SL}} = S - |\tau_{12}|$, and the bi-linear interface constitutive law used to calculate the longitudinal tensile strength of the UD ply as described in Section 2.2 will be updated accordingly (as shown in Figure 5a); this reduction of the available shear stresses from S to $S_{\mathrm{SL}} < S$ will thus lead to a reduction of the residual longitudinal tensile strength (as calculated in Section 2.2) from $X_{\mathrm{D}}^{\mathrm{T}}$ to a new value $\sigma_1 < X_{\mathrm{D}}^{\mathrm{T}}$. By varying S_{SL} from 0 to S, a new failure envelope considering the interaction between longitudinal tensile failure and transverse shear failure is generated

(see curve with $\sigma_2 = 0$ in Figure 6a).

In order to extend the interaction between longitudinal tension (σ_1) and transverse shear (τ_{12}) to transverse tension (σ_2), consider the matrix/interface dominated (σ_2 vs. τ_{12}) failure envelope from LaRC05 [22], given as

$$F_{\text{Im}} \equiv \sqrt{\left(\frac{m^* \cdot \bar{\gamma}}{|S^{\text{is}}| - m^* \cdot \eta \cdot \bar{\beta}}\right)^2 + \left(\frac{m^* \cdot \langle\bar{\beta}\rangle_+}{Y_{\text{T}}^{\text{is}}}\right)^2} = 1, \tag{6}$$

where $\langle\beta\rangle_+ = \beta$ if $\beta > 0$ and $\langle\beta\rangle_+ = 0$ if $\beta \leq 0$. This requires defining the friction coefficient η, and in-situ tensile and shear strengths Y^{is} and S^{is} (calculated assuming thick laminates) as [22]

$$\eta = -\frac{S}{Y^{\text{C}}} \cdot \frac{\cos(2\alpha_0)}{\cos(\alpha_0)^2}; \quad Y^{\text{is}} = 1.12 \cdot \sqrt{2} \cdot Y^{\text{T}}; \quad S^{\text{is}} = \sqrt{2} \cdot S, \tag{7}$$

where α_0 is the angle of fracture surfaces formed under pure transverse compression (which is set to $53°$ in this study from experimentally measured values [22]). Although, in this study, no compressive failure is considered, the friction coefficient η in the first term of F_{Im} is preserved from the original LaRC05 criterion [22], which predicts a reduction of the apparent shear strength of a UD ply under transverse tension and leads to a non-quadratic tension-shear failure envelope, as represented in Eq. 6.

Using this failure criterion for interfacial failure (represented in Figure 6b), the interaction between σ_1 and τ_{12} described previously is naturally extended to any combination of in-plane stresses $\{\sigma_1, \sigma_2, \tau_{12}\}$ (see Figure 6); this generates the longitudinal-tension/transverse-tension/shear failure surface shown in Figure 6c. Because this failure surface must be calculated numerically, a finite number of N_{p} points is considered along the σ_2 and τ_{12} axes; the failure surface is subsequently interpolated for any local loading vector $[\bar{\alpha} \; \bar{\beta} \; \bar{\gamma}]^{\text{T}}$ to determine the local failure factor m^* of each ply in the equivalent laminate.

2.4. Homogenisation of laminate strength of a quasi-isotropic layup

2.4.1. Relationships between laminate and ply stress-fields and failure

For any global loading unit vector (defined by $\widehat{\boldsymbol{\sigma}}_{\text{g}} = [\bar{A}, \bar{B}, \bar{\Gamma}]^{\text{T}}$), failure of the equivalent laminate (assumed to have N_{ply} plies) is defined by the global failure factor M^*. Two different methods are proposed to calculate M^*: a ply-discount method (Section 2.4.2) and a strain-energy approach (Section 2.4.3). For both methods it is assumed that, for the loading direction $\widehat{\boldsymbol{\sigma}}_{\text{g}}$ defined, the local stress vector $\widehat{\boldsymbol{\sigma}}_{\text{l}}$ of a ply with orientation θ_i can be calculated through classical laminate theory (Eq. 5), and that the local failure factor for each ply $m^*(\theta_i)$ can be calculated by the ITS criterion described in Section 2.3.2.

2.4.2. Ply-discount method

In the Ply-Discount Method (PDM), the global proportional loading factor M applied to the laminate is progressively increased until a ply with orientation θ_i fails (i.e. until $m(\theta_i) = m^*(\theta_i)$ is

reached), and then the local stiffness matrix $\mathbf{Q}_{l,i}$ of the damaged ply is reduced by the damage variable d [31, 32]:

$$\mathbf{Q}_{l,i}(m(\theta_i) \geq m^*(\theta_i)) = \begin{pmatrix} (1-d)Q_{11} & (1-d)Q_{12} & 0 \\ (1-d)Q_{21} & (1-d)Q_{22} & 0 \\ 0 & 0 & (1-d)G_{12} \end{pmatrix}, \tag{8}$$

The global stiffness matrix $\mathbf{Q}_g$ is updated accordingly, which redistributes the stresses in each ply (Eq. 5). This process is repeated until the updated loading factor M in the laminate falls below 90% of the maximum factor found so far: this event defines failure of the laminate, and $M \equiv M^*$.

Assuming brittle ply failure, the damage variable d should ideally be equal to 1 to fully degrade the stiffness in a failed ply; however, in order to avoid singular stiffness matrices, we used $d = 0.9$ throughout this study (it will be confirmed in Section 3 that the results from the model are not sensitive to the value of d, as long as it is reasonably close to 1).

If the equivalent laminate always fails as soon as the first ply fails, a First-Ply-Failure (FPF) approach can be used to replace the PDM, to improve the computational efficiency by avoiding recalculating stiffness matrices. For the FPF approach, the failure stress of each ply i is firstly determined through the local stress factor $m^*(\theta_i)$ (calculated from Section 2.3.2). The ply that fails with the smallest $m^*(\theta_i)$ is identified, and the global failure factor of the laminate is calculated as

$$M^* = \min\{m^*(\theta_i)\}, \quad i = \{1, 2, ..., N_{\text{ply}}\}. \tag{9}$$

2.4.3. Energy approach

Although the PDM proposed in Section 2.4.2 is physically-based, it requires calculating the stress state $\widehat{\boldsymbol{\sigma}}_l$ and the local loading factor m^* for each ply of the equivalent laminate, and updating $\widehat{\boldsymbol{\sigma}}_l$ and m^* when each ply fails, until all N_{ply} plies of the EL fail. Consequently, this method requires relatively long computations. The computational cost of the PDM can be reduced by assuming a FPF criterion (in which case the calculation of $\widehat{\boldsymbol{\sigma}}_l$ and m^* only need to be carried out once, for the pristine laminate), but the assumption of ultimate failure in the EL when first ply fails may not always hold.

It is therefore of interest to analyse alternative failure criteria which are simultaneously (i) more computationally-efficient than the PDM and (ii) more global than the FPF method. Such an alternative phenomenologically-based analytical method is here proposed, which requires analysing the strain energies of the EL at the pristine stage and calculating local failure factors m^* once only. This method assumes that the strain energy required for the equivalent laminate to fail is the same as the sum of strain energies required for each ply to fail.

For each ply with orientation θ_i, the local specific strain energy at failure U_l^* is calculated assuming a fully linear-elastic response as follows ($\mathbf{S} = \mathbf{Q}^{-1}$ is the compliance matrix):

$$U_l^*(\theta_i) = \frac{1}{2} \cdot [\boldsymbol{\sigma}_l^*(\theta_i)]^{\text{T}} \cdot \boldsymbol{\varepsilon}_l^*(\theta_i) = \frac{1}{2} \cdot [\boldsymbol{\sigma}_l^*(\theta_i)]^{\text{T}} \cdot \mathbf{S}_l(\theta_i) \cdot \boldsymbol{\sigma}_l^*(\theta_i) = \frac{1}{2} \cdot m_i^{*2} \cdot [\widehat{\boldsymbol{\sigma}}_l(\theta_i)]^{\text{T}} \cdot \mathbf{S}_l(\theta_i) \cdot \widehat{\boldsymbol{\sigma}}_l(\theta_i). \tag{10}$$

11

Consequently, from the total energy U_g^* required for N_{ply} plies to fail, the relation between global and local failure factors (respectively M^* and m_i^*) becomes

$$U_g^* = \sum_{i=1}^{N_{\text{ply}}} U_l^*(\theta_i) \Leftrightarrow \frac{1}{2} \cdot M^{*2} \cdot [\widehat{\boldsymbol{\sigma}}_g]^{\text{T}} \cdot \mathbf{S}_g \cdot \widehat{\boldsymbol{\sigma}}_g = \frac{1}{2} \cdot \sum_{i=1}^{N_{\text{ply}}} m_i^{*2} \cdot [\widehat{\boldsymbol{\sigma}}_l(\theta_i)]^{\text{T}} \cdot \mathbf{S}_l(\theta_i) \cdot \widehat{\boldsymbol{\sigma}}_l(\theta_i). \qquad (11)$$

Eq. 11 equates the *total energies* required to fail (i) the equivalent laminate and (ii) all of its plies.

It has been shown that most materials have different levels of sensitivity to different components of the stress tensor. This concept has been applied to conventional composites [33] considering relatively complex decompositions of the stress tensor in a UD ply, but the most well-known and widely-used failure criterion based on selected components of the stress tensor is the Von Mises criterion, based on the deviatoric component of the stresses. For this reason, it is also interesting to consider a decomposition of the total energy criterion defined in Eq. 11, for instance, into deviatoric and volumetric components. Using Felippa's rigidtropic model [34] for anisotropic materials, the deviatoric (subscript $_{\text{dev}}$) and volumetric (subscript $_{\text{vol}}$) components of the stresses and strains can be calculated using the smallest eigenvector $\mathbf{v}$ of the compliance matrix $\mathbf{S}$ as

$$\sigma_{\text{vol}} = \frac{1}{3}\mathbf{v}^{\text{T}}\boldsymbol{\sigma}; \qquad \varepsilon_{\text{vol}} = \mathbf{v}^{\text{T}}\boldsymbol{\varepsilon} = \mathbf{v}^{\text{T}} \cdot (\mathbf{S} \cdot \boldsymbol{\sigma});$$

$$\boldsymbol{\sigma}_{\text{dev}} = \boldsymbol{\sigma} - \mathbf{v}\sigma_{\text{vol}}; \quad \boldsymbol{\varepsilon}_{\text{dev}} = \boldsymbol{\varepsilon} - \frac{1}{3}\mathbf{v}\varepsilon_{\text{vol}} = \boldsymbol{\varepsilon} - \frac{1}{3}\mathbf{v} \cdot (\mathbf{S}_{\text{vol}} \cdot \boldsymbol{\sigma}_{\text{vol}}). \qquad (12)$$

Therefore, the strain energy can be decomposed as

$$U_g = U_{\text{dev}} + U_{\text{vol}}, \quad \text{where} \quad U_{\text{vol}} = \frac{1}{2}\sigma_{\text{vol}} \cdot \varepsilon_{\text{vol}} \quad \text{and} \quad U_{\text{dev}} = \frac{1}{2}\boldsymbol{\sigma}_{\text{dev}}^{\text{T}} \cdot \boldsymbol{\varepsilon}_{\text{dev}}. \qquad (13)$$

This decomposition can be used assuming that ultimate failure occurs when either the *deviatoric* or the *volumetric* component of the energy reaches the critical level (as defined by a component-based version of Eq. 11), taking $M^*(\widehat{\boldsymbol{\sigma}}_g) = \min\{M_{\text{dev}}^*(\widehat{\boldsymbol{\sigma}}_g), M_{\text{vol}}^*(\widehat{\boldsymbol{\sigma}}_g)\}$. This decomposition of the strain energy is applied both at the local (i.e. for each UD ply) and global (i.e. for the full EL) scales; mathematically, this is done by replacing the full stress vectors shown in Equation 11 with their volumetric or deviatoric components, both for the global (on the left-hand-side) and local (on the right-hand-side) sides of the equation.

The energy criteria proposed in this section do not require any updates to the global or local stiffness matrices, which makes the energy criteria more computationally efficient than the PDM proposed in Section 2.4.2. Moreover, the energy criteria depend on the local failure factor of all plies in the equivalent laminate, in contrast with the FPF criterion (Eq. 9), which only depends on the local failure factor of the weakest (i.e. with the lowest failure strain) ply. The influence of the macro-scale failure criterion on the strength of the equivalent laminate will also be shown in Section 3.2.3.

3. Results

3.1. Model implementation and inputs

The model was implemented in Matlab [37]. The results shown in this section will be based on HexMC-M77 [35] materials, with tow geometries identified in Table 1.

Table 2 shows the properties of the UD prepregs with same fibre and matrix type as the tows of the HexMC-M77 materials [35] analysed. It is noticed that the fibre volume fraction of the UD prepreg

($V_{\mathrm{f,UD}}$) and that of the corresponding TBDCs ($V_{\mathrm{f,TBDC}}$) are different; therefore, the longitudinal properties of the UD prepreg ($E_{1,\mathrm{UD}}$ and $X_{\mathrm{UD}}^{\mathrm{T}}$) shown in Table 2 were subsequently corrected for this discrepancy in the fibre volume fraction according to a simplified rule of mixture:

$$E_{1,\mathrm{UD,TBDC}} = E_{1,\mathrm{UD}} \cdot \frac{V_{\mathrm{f,TBDC}}}{V_{\mathrm{f,UD}}}, \quad X_{\mathrm{UD,TBDC}}^{\mathrm{T}} = X_{\mathrm{UD}}^{\mathrm{T}} \cdot \frac{V_{\mathrm{f,TBDC}}}{V_{\mathrm{f,UD}}}, \tag{14}$$

where $E_{1,\mathrm{TBDC}}$ and $X_{\mathrm{UD,TBDC}}^{\mathrm{T}}$ stand for the corrected modulus and strength respectively, used as inputs for the model.

The numerical parameters used to run the model are listed in Table 3. The values of these numerical parameters were selected through convergence studies, to make sure that the model converges while maintaining computational efficiency. The orientations of the plies considered in the quasi-isotropic ELs are equally-spaced by $\Delta\theta = 180°/N_{\mathrm{ply}}$, such that $\theta_1 = 0°, \theta_2 = 180°/N_{\mathrm{ply}}, ..., \theta_{N_{\mathrm{ply}}} = 180° \cdot (N_{\mathrm{ply}} - 1)/N_{\mathrm{ply}}$.

3.2. Model results at different scales

3.2.1. Model results for the longitudinal tensile strength of a UD discontinuous ply

Figure 7 shows the uni-axial strength of a UD discontinuous ply ($X_{\mathrm{D}}^{\mathrm{T}}$) predicted by the stochastic shear-lag model described in Section 2.2 for two tow thicknesses t_{t} and two tow aspect ratios R, where R is defined by $R = l_{\mathrm{t}}/t_{\mathrm{char}}$. The effect of two common modelling assumptions — (i) perfect staggering

of the tows and (ii) perfect-plastic interface ($\mathcal{G}_{\mathrm{IIc}} \to \infty$) — is also analysed. Figure 7 shows that:

1. If the model is simplified to assume perfect staggering of the tows, each overlap between the tows has length $\bar{l}_{\mathrm{o}} = l_{\mathrm{t}}/2$ and thickness $\bar{t}_{\mathrm{o}} = t_{\mathrm{char}}$, and hence the stresses transferred by all overlaps are uniform. However, TBDCs have a random location of tow-ends, thus creating shorter overlaps that can only transfer a fraction of the stresses of longer overlaps (see Figure 5b), which is not

captured by the perfect-staggering assumption. Consequently, assuming perfect tow staggering (as often done in the literature [15]) leads to over-predicting the strength of a UD discontinuous ply ($X_{\mathrm{D}}^{\mathrm{T}}$), and hence over-predicting the strength of TBDCs.

2. Assuming a perfectly-plastic behaviour at the interface of the overlaps between the tows also leads to a significant over-prediction of $X_{\mathrm{D}}^{\mathrm{T}}$. This is due to not considering the finite fracture tough-

ness of the tow interface, and hence ignoring the failure mechanism of brittle interfacial/matrix cracking.

3. Moreover, considering both strength and fracture toughness criteria for the failure of the tow interface (as done in the "full model"), $X_{\mathrm{D}}^{\mathrm{T}}$ is mostly dependent of the absolute value of the tow thickness; in contrast, when a "perfect-plastic interface" is assumed (i.e. when the fracture toughness of the tow interface is assumed to be infinite), $X_{\mathrm{D}}^{\mathrm{T}}$ is mostly dependent on the aspect ratio R of the tow.

3.2.2. Model results for the failure envelopes of a UD discontinuous ply and an equivalent laminate

Figure 8 compares the failure envelopes for a UD discontinuous ply ($t_{\mathrm{t}} = 0.164$ mm) generated by the ITS criterion and by two commonly-used failure criteria from the literature — Tsai-Wu [19] and LaRC05 [22] criteria. The LaRC05 and ITS criteria consider the in-situ effect on the ply strengths (see Eq. 7); consequently, their failure envelopes intersect the axes at larger stresses compared to Tsai-Wu's criterion (which uses un-modified strengths).

Figure 9 shows that, compared to the ITS criterion, the LaRC05 criterion overpredicts the uni-axial tensile strength of TBDCs only slightly, as it assumes no interaction between longitudinal tension and transverse and shear stresses. For a TBDC under uni-axial loading, failure of the most critical plies is dominated by longitudinal stress σ_1 (see Figure 10) and, therefore, the influence of the tension-shear interaction is small (which justifies the similarity between the results from the ITS and LarC05 criteria).

Figure 10 shows the stress components in the plies of an EL under uni-axial loading, at the moment of first ply failure. The ply with orientation of 14° has the most critical loading case, and thus its stress state falls exactly on the failure surface shown in Figure 6c, mostly due to the contribution of σ_1 and τ_{12}. The other plies with orientation near 14° are also very close to failure (see Figure 10d); this indicates that, as soon as the 14°-ply fails, there will be a significant overload transferred to the other plies with a similar orientation, which can cause catastrophic failure. This indicates that failure of the EL can be governed by first ply failure, as will be discussed in the next section.

3.2.3. Results from macro-level models

Figure 11 compares the strengths of equivalent laminates predicted by the ply-discount method (PDM), first-ply failure method (FPF), total energy approach (TEA), and decomposed energy approach (DEA), and against experimental results [7]. PDM and FPF give exactly the same result, meaning that the PDM predicts failure of the equivalent laminate once the weakest ply fails (this is verified with all loading cases; it will be shown in Section 3.4 that the first ply failing in the equivalent laminate is well-aligned with the main loading direction (meaning that it carries a large proportion of

14

the load), which justifies the good agreement between FPF and PDM. This explains why the PDM model is not sensitive to the damage variable d (see Section 2.4.2); however, this does not imply that TBDCs fail when first failure initiates, as damage accumulation through pull-out and failure of individual tows in a UD ply is considered in the micro-scale model (see Section 2.2).

The PDM and FPF criteria show a much better agreement with the experimental data than the energy approaches (the total energy approach overestimates the experimental strength, while the decomposed energy approach underestimates the experimental strength). Because the PDM and FPF have the same accuracy, and the FPF is much more computationally efficient than the PDM, all the results shown hereafter will consider the FPF method.

3.2.4. Comparison to experimental data

Figure 12 shows a good agreement between the modelling results and the experimental data for equivalent laminates with quasi-isotropic (QI) lay-ups. The discrepancy between the QI equivalent laminates and Random Composites (RCs) arises from the intrinsic variability in the microstructure of random TBDCs [7]. The fact that the same failure mechanisms have been experimentally observed in QI ELs and in RCs suggests that this modelling framework can be extended to predict the strength of RCs as well. Such extension needs to account for the intrinsic variability in the microstructure of random TBDCs [7]; this will be further illustrated in Section 3.3.2.

3.3. Further modelling capabilities

3.3.1. Failure envelope for TBDC under in-plane bi-axial loading

Figure 13a shows the failure envelope predicted from the model for TBDCs under in-plane bi-axial loading. Figure 13b shows the orientation of the first failed ply (θ^*) against the loading ratio between longitudinal and transverse load (defined by $\delta = \arctan(\sigma_x/\sigma_y)$). It is noticeable that, as the loading ratio changes, the orientation of the most critical ply (which determines failure of the equivalent laminate) also changes. However, experimental measurement of the strength and failure mechanisms of TBDCs under more than one stress component are still not available in the literature, and therefore these predictions cannot be validated.

3.3.2. Predicting the local strength of TBDCs with a known local microstructure

The model proposed in this study is also capable of predicting the local strength of TBDCs, at points with a known microstructure. To illustrate this, we calculated the local strength of two randomly-oriented TBDC plates as follows:

1. Defined the local number of tows ($N_{\mathrm{ply}}(x,y)$) in the through-the-thickness direction and the local tow orientations $\{\theta_1(x,y), \theta_2(x,y), ..., \theta_{N_{\mathrm{ply}}(x,y)}\}$ at each point of two randomly-oriented TBDC

15

plates (which have been manufactured with a method purposely developed to track the local microstructure at each point of the grid [7]).

2. Calculated the strength of the equivalent laminate at each point (x, y) in the plate, considering that the plies in the equivalent laminate have the same orientations of the tows $\{\theta_1, \theta_2, ..., \theta_{N_{\mathrm{ply}}}\}$ at that point.

3. Repeated Step 2 for all points in the plate, thus defining a local strength map.

4. Corrected the strength calculated as described above, according to the local fibre volume fraction $V_{\mathrm{f}}(x, y)$. The local fibre volume fraction was estimated using the rule of mixture, considered that $V_{\mathrm{f}}(x, y)$ has a linear relationship with the number of tows in the through-the-thickness direction of the plate:

$$V_{\mathrm{f}}(x, y) = (N_{\mathrm{ply}}(x, y) - \overline{N_{\mathrm{ply}}}) \cdot \frac{\Delta V_{\mathrm{f}}}{2} + \overline{V_{\mathrm{f}}}, \tag{15}$$

where $\overline{N_{\mathrm{ply}}}$ is the mean of $N_{\mathrm{ply}}(x, y)$ for all grid points in the plate, $\overline{V_{\mathrm{f}}}$ is the nominal fibre volume fraction in the plate, and $\Delta V_{\mathrm{f}} = V_{\mathrm{f,max}} - V_{\mathrm{f,min}}$, where $V_{\mathrm{f,max}}$ and $V_{\mathrm{f,min}}$ are respectively the maximum and minimum values of the local fibre volume fraction, measured experimentally in the plate (75% and 44% for the thick-prepreg plate, and 68% and 49% for the thin-prepreg plate [7]).

Figure 14 maps the local strength (calculated through the method described above) to the failure region of TBDC specimens tested experimentally [7] under uni-axial tensile loading. It is not possible to define a clear relationship between the location of failure and the local strengths, mostly due to the high variability which is intrinsic of TBDCs, which would require a large number of specimens tested to provide statistically significant results. Moreover, the present model is able to predict failure

initiation at a point with a known microstructure, but this is not sufficient to predict the location of the final fracture surface of a specimen. Nevertheless, the tendency for failure to occur in the regions with lower strength (especially for the thick-prepreg material) shows that the proposed model may be suitable not only to predict the magnitude of the strength of TBDCs, but also to predict the potential location of failure in specimens or structures with a known microstructure.

Figures 14a and 14c consider that $\Delta V_{\mathrm{f}} = 0$ (i.e. neglect variations in the local fibre content), and Figures 14b and 14d consider that $\Delta V_{\mathrm{f}} = V_{\mathrm{f,max}} - V_{\mathrm{f,min}}$ (i.e. consider the same variability in fibre content as observed experimentally). By considering the variability in local fibre volume fraction in addition to the random tow orientations, a higher variability in the strength of TBDCs was found in Figures 14b and 14d than in Figures 14a and 14c. However, the location of the regions with

extreme strengths (i.e. much higher/lower strength than average) does not change significantly with the correction for the local fibre volume fraction; this shows that the local strength is not highly sensitive to reasonable variations in the local fibre volume fraction, which supports the assumption

16

made in Step 4 above.

3.4. Failure mechanisms of TBDCs

Figure 15 shows that the strength of TBDCs is governed by two different failure mechanisms:

1. When the remote stress for tow fracture is lower than the remote stress for failure of the tow interface, failure of TBDCs is dominated by tow fracture (see Figure 15d). In this case, the most critical ply in the EL will be the 0° ply (see Figure 15c); therefore, improving the tow strength improves the strength of the 0° ply and, consequently, improves the strength of the TBDC (see Figure 15b).

2. When the remote stress for tow fracture is higher than the the remote stress for failure of the tow interface, failure of TBDCs is dominated by tow pull-out (see Figure 15d). In this case, the most critical ply in the EL is oriented at approximately 14° with the overall load direction (see Figure 15c; improving the mode-II fracture toughness at the interface improves the strength of the TBDC (see Figure 15a); this also highlights that it is vital to account for the finite fracture toughness of the tow interface when attempting to predict the strength of TBDCs.

For both thin- and thick-prepreg RCs, a combination of tow fracture and tow pull-out has been observed experimentally on fracture surfaces, but with a significantly higher predominance of tow fracture in the thin-prepreg RC than in their thick-prepreg counterpart [7]. The model predictions are in agreement with this trend (see Figure 15d).

The fluctuation seen in the orientation of the critical ply θ^* (Figure 15c) in the TBDC is due to the very similar ratio between the magnitude of the applied stress state (m) and the magnitude of the critical stress state (m^*) of plies with a similar orientation θ, as shown in Figure 10d.

4. Discussion

4.1. Capabilities of the proposed modelling approaches

By comparing the modelling results with experimental data (Figure 12), it is found that:

- The full multi-scale strength model — considering a micro-scale stochastic shear-lag model, a meso-scale interactive-tension-shear criterion, and a macro-scale ply discount method for the equivalent laminate — accurately predicts the strength of a quasi-isotropic equivalent laminate with discontinuous tows. The predictions of the model for QI ELs overpredict the strength of the corresponding randomly-oriented TBDCs, because QI ELs do not feature the variability present in the microstructure of random TBDCs [7], which leads to premature failure of the latter.

- The micromechanical stochastic shear-lag model is physically sound, as it accounts for both (i) brittle interfacial cracking and (ii) the random location of tow-ends. Neglecting the former effect

and assuming a perfectly-plastic stress transfer at the interface between the tows (as done in Kelly-Tyson's model [14]) is clearly not suitable for TBDCs, as doing so would suggest that the strength of TBDCs is virtually unaffected by the thickness of the tows for a constant tow aspect-ratio (Figure 7), which is contradicted by experimental evidence [1, 15]. Considering these two features also allows the model to capture the failure mechanisms (tow failure and tow debonding) of TBDCs under tension, as shown in Figure 15d.

- Considering the interaction between longitudinal and transverse loading, as done in the ITS criterion, reduces slightly the predicted uni-axial strength of TBDCs when compared to failure criteria which were developed for CFCs and thus neglect this interaction (e.g. LaRC05). For the TBDCs analysed in this study, the influence of the interaction between longitudinal and other stress components is small, because the stress state of the critical ply that triggers failure of the EL is dominated by longitudinal stresses (see Figure 10); however, the effect of this interaction could be more significant when considering other material systems.

- The strength model proposed in this paper can be used to predict the full strength map (see Figure 14) of a structure made with TBDCs, based on the local microstructure (as long as the tows are mostly oriented in a 2D plane). Therefore, the proposed model can be used to identify failure initiation in a Monte-Carlo simulation of TBDC structures, as long as the variability of their microstructure is known. Neverthless, it is clear that such Monte-Carlo simulation would require further developments additional to the proposed models, in order to predict how failure would propagate in a material with such heterogeneous strength fields as the ones shown in Figure 14.

- The proposed model has been used to estimate the bi-axial strength of TBDCs under two or three in-plane stress components (see Figure 13a), although further experiments need to be carried out to validate the failure envelopes predicted.

4.2. Novelty and key features of the model

This model is the first attempt in the literature to provide physically-based predictions for the tensile strength and tension-tension/tension-shear failure envelopes of DFCs in general, and TBDCs in particular. In addition, the key novel features of the proposed model relatively to the existing literature on DFCs and TBDCs [1, 11, 13, 14, 27, 38] are the following:

- The model uses a bi-linear interfacial constitutive law considering both strength-dominated and toughness-dominated failure criteria, hence taking into account brittle interfacial cracking, which is likely to occur in TBDCs due to the large dimensions of the tows.

- The model considers a stochastic distribution of overlap-lengths and overlap-thicknesses, and hence takes into account the random location of the tows in the microstructure of discontinuous composites.

18

- The model considers the interaction between longitudinal and transverse stress components in a UD discontinuous composite ply based on the physics of tow pull-out. In contrast, the failure criteria most currently-used in the literature consider either no interaction between longitudinal and transverse failure [21–23], or a non-physically-based interaction [19, 20].

- The model allows a significant reduction in computational cost compared to conventional FE simulations of RVEs (which can take four hours of CPU time to complete the analysis of a single loading case [29]). In comparison, our model requires approximately 300 seconds to predict the full failure envelope (as shown in Figure 13a) of a TBDC material, using the FPF macro-scale criterion (which was validated against the PDM) and thee numerical parameters shown in Table 3.

Compared to Feraboli's model [16] specifically aimed at TBDCs, the model proposed in this paper shares the stochastic laminate analogy and a physically-based FPF method; it advances from Feraboli's model [16] by taking into account the discontinuities in the material architecture, thus predicting a mixture of tow fracture and tow pull-out as observed in experiments [15]. This model also shares the multi-scale approach with Harper's model [1], but considers more physically-sound criteria at all scales (stochastic non-linear shear-lag model at the micro-scale, ITS failure criterion at the meso-scale, and PDM at the macro-scale). Compared to Selezneva's analytical strength model for TBDCs [27], which generates a full 2D microstructure with the random orientation and location of the tows in one through-the-thickness slice of the material, our model considers the 3D microstructure of the tows, which takes into account the effect of tow width.

4.3. Optimisation and performance of TBDCs

There are two main failure mechanisms observed in TBDCs and predicted by the model: tow fracture — governed by the tensile strength of the tows/prepreg — and tow pull-out — governed by the fracture toughness of the interface between the tows. Therefore, the strength of TBDCs can be improved by:

- Improving the tensile strength of the tows, and therefore increasing the remote stress for tow fracture to occur. However, Figure 15b shows that this is effective only when tow fracture is the dominating failure mechanism, which occurs if the tensile strength of the tows is relatively low.

- Improving the mode-II fracture toughness of the interface between the tows, which would delay the onset of delamination between the tows and, consequently, reduces the proportion of tow pull-out (see Figure 15a).

- Considering tow geometry, the model suggests that using thinner tows would be an effective method to promote the stress-transfer and delay delamination between tows in TBDCs (see Figure 12). This agrees with experimental research showing that thin-ply TBDCs are stronger than their standard-

19

or thick-ply counterparts [7, 39, 40].

5. Conclusions

This work proposed a model for predicting the tensile strength and failure envelopes of TBDCs, and assessed the influence of several model features on the quality of the predictions. The full model takes into account several features not previously considered in combination in the literature [1, 26, 27]: (i) the multi-scale architecture of the material; (ii) the possibility of tow pull-out by brittle delamination of the interface between the tows, as well as by progressive interfacial yielding; (iii) the stochastic distribution of the location of the tow-ends; and (iv) the interaction between longitudinal loading and shear/transverse loading (which dominate tow pull-out and interface failure respectively). The main conclusions that can be drawn from this work are the following:

1. The model assessed the effect of considering different mechanisms/features to predict the strength of TBDCs:

    (a) At the micro-scale, considering the random location of tow-ends allows the combination of tow-fracture and tow pull-out to be predicted. Moreover, considering the finite mode-II fracture toughness of the interface between tows allows brittle cracking of the interface to be predicted, which allows for the effect of tow thickness on the strength of TBDCs to be captured.

    (b) At the meso-scale, the predicted failure envelopes considering the interaction between longitudinal and transverse and shear stress components show a small deviation from the criteria that do not account for this interaction.

    (c) At the macro-scale, first ply failure and ply discount methods predict the same result for the equivalent laminate, hinting that the laminate fail as soon as the first ply fails. Approaches based on overall energies either overestimated (TEA) or underestimated (DEA) the strength of TBDCs.

2. The model is able to capture the effect of tow thickness on the tensile strength of TBDCs, and suggests that TBDCs can be optimised for a higher strength by decreasing the tow thickness. Improving the longitudinal tensile strength of the tows and/or the mode-II fracture toughness of the matrix or tow interface could also improve the strength of TBDCs.

3. The model proposed was validated against experiments made with quasi-isotopic equivalent laminates with a discontinuous microstructure.

4. The models developed are able to populate failure envelopes for TBDCs in a computationally efficient way, and to predict local strength maps for TBDC structures taking the intrinsic variability of the microstructure into account, although more comprehensive experimental data is

20

needed for full validation. Further work is therefore required before a modelling framework for TBDCs can be confidently applied in structural design.

Acknowledgements

Appendix A. Simplification of the non-linear shear-lag model considering a bi-linear interfacial law

The stress-strain response of an overlap between neighbouring tows (as shown in Figure 4) is calculated based on Pimenta and Robinson's shear-lag model [15], but assuming a bi-linear tow interface law (Figure 5a). This law is composed by three subdomains: the elastic subdomain [1], the strain-softening subdomain [2], and the fully-debonded subdomain [3].

As the overlapping region is progressively loaded (i.e. increasing ε_o and σ_o), the shear strains in the tow interface progressively increase. The subdomains of the constitutive law of the tow interface which are active in the overlap evolve according to the following possibilities (note that the numbers between the square brackets represent the active subdomains of the interface constitutive law, and the transition points at which new subdomains are activated are shown above the arrows):

1. $[1] \xrightarrow{\text{Point1:}\{\varepsilon_\mathrm{o}(1),\ \sigma_\mathrm{o}(1)\}} [1\ 2] \xrightarrow{\text{Point2:}\{\varepsilon_\mathrm{o}(2),\ \sigma_\mathrm{o}(2)\}} [2] \to [3]$,

   for $l_\mathrm{o} \leq l_\mathrm{crit}$ (interface yielding);

2. $[1] \xrightarrow{\text{Point1:}\{\varepsilon_\mathrm{o}(1),\ \sigma_\mathrm{o}(1)\}} [1\ 2] \xrightarrow{\text{Point2:}\{\varepsilon_\mathrm{o}(2),\ \sigma_\mathrm{o}(2)\}} [1\ 2\ 3] \xrightarrow{\text{Point3:}\{\varepsilon_\mathrm{o}(3),\ \sigma_\mathrm{o}(3)\}} [2\ 3] \to [3]$,

   for $l_\mathrm{o} > l_\mathrm{crit}$ (interface cracking),

where the critical length (defining the transition between plastic yielding and brittle cracking of the tow interface) is defined as $l_\mathrm{crit} = \dfrac{\pi}{2 \cdot S}\sqrt{t_\mathrm{o} \cdot E_1 \cdot \mathcal{G}_\mathrm{IIc}}$.

One can calculate (analytically) the remote stress (σ_o) and strain (ε_o) which are applied to the overlap when the active interface subdomains change; the corresponding expressions are shown in

21

Table A.4. With these analytical stress-strain points defined, a stress-strain curve (σ_{o} vs. ε_{o}) for each overlap length $l_{\mathrm{o}} \in [0, l_{\mathrm{t}}]$ and for each overlap thickness $t_{\mathrm{o}} \in [0, 2 \cdot t_{\mathrm{char}}]$ can be populated:

(a) When only subdomain [1] is active, $\sigma_{\mathrm{o}} = E_{\mathrm{o}} \cdot \varepsilon_{\mathrm{o}}$, where $E_{\mathrm{o}} = \sigma_{\mathrm{o}}(1)/\varepsilon_{\mathrm{o}}(1)$;

(b) When subdomains [1 2] are active, the stress-strain curve of the overlap is approximated by a quadratic fitting $\sigma_{\mathrm{o}}(\varepsilon_{\mathrm{o}}) = a \cdot \varepsilon_{\mathrm{o}}^2 + b \cdot \varepsilon_{\mathrm{o}} + c$; the constants a, b and c are found considering the following boundary conditions:

$$\sigma_{\mathrm{o}}(\varepsilon_{\mathrm{o}}(1)) = \sigma_{\mathrm{o}}(1), \quad \sigma_{\mathrm{o}}(\varepsilon_{\mathrm{o}}(2)) = \sigma_{\mathrm{o}}(2), \quad \frac{\mathrm{d}\sigma_{\mathrm{o}}}{\mathrm{d}\varepsilon_{\mathrm{o}}}(\varepsilon_{\mathrm{o}}(1)) = \frac{\sigma_{\mathrm{o}}(1)}{\varepsilon_{\mathrm{o}}(1)}; \tag{A.1}$$

(c) When subdomains [1 2 3] are active, the overall stress plateaus at the fracture mechanics strength, so that $\sigma_{\mathrm{o}}(3) = \sqrt{\dfrac{E_1 \cdot \mathcal{G}_{\mathrm{IIc}}}{t_{\mathrm{o}}}}$, and $\varepsilon_{\mathrm{o}}(3)$ is as shown in Table A.4.

References

[1] L. T. Harper. *Discontinuous carbon fibre composites for automotive applications.* PhD thesis, University of Nottingham, 2006.

[2] P. Feraboli, E. Peitso, F. Deleo, T. Cleveland, and P. B. Stickler. Characterization of prepreg-based discontinuous carbon fiber/epoxy systems. *Journal of Reinforced Plastics and Composites*, 28(10):1191–1214, 2009.

[3] S. Pimenta, A. Ahuja, and A. Yong. Damage tolerant tow-based discontinuous composites. 20th International Conference on Composite Materials; Copenhagen, Denmark, 19-24 Jul 2015.

[4] Nordam pioneers HexMC composite window frames for Boeing 787 dreamliner. `http://www.asdnews.com/news-11358/Nordam_Pioneers_Hexmc_Composite_Window_Frames_for_Boeing_787_Dreamliner.htm`, Feb 2007. Accessed: 2016-01-30.

[5] P. Feraboli, F. Gasco, and B. Wade. Lamborghini "forged composite" technology for the suspension arms of the sesto elemento. Montreal, Quebec, Canada, 26 - 28 September 2011. 26th Annual Technical Conference of the American Society for Composites 2011: The 2nd Joint US-Canada Conference on Composites.

[6] P. Dave. What is forged composite: a new way of using carbon fibre. `http://www.carbonfibergear.com/what-is-forged-composite-a-new-way-of-using-carbon-fiber`, Oct 2010. Accessed: 2016-01-30.

[7] Y. Li, S. Pimenta, J. Singgih, S. Nothdurfter, and K. Schuffenhauer. Experimental investigation of randomly-oriented tow-based discontinuous composites and their equivalent laminates. *Composites: Part A - Applied Science and Manufacturing*, 102:64–75, 2017.

[8] Y. Wan and J. Takahashi. Tensile properties and aspect ratio simulation of transversely isotropic discontinuous carbon fiber reinforced thermoplastics. *Composites Science and Technology*, 137(2016):167–176, 2016.

[9] M. Selezneva and L. Lessard. Characterization of mechanical properties of randomly oriented strand thermoplastic composites. *Journal of Composite Materials*, 50(20):2833–2851, 2015.

[10] S. G. Advani. The use of tensors to describe and predict fiber orientation in short fiber composites. *Journal of Rheology*, 31(1987):751, 1987.

[11] F. W. J. Van Hattum and C. A. Bernardo. A model to predict the strength of short fiber composites. *Polymer Composites*, 20(4):524–533, 1999.

[12] M. Hashimoto, T. Okabe, T. Sasayama, H. Matsutani, and M. Nishikawa. Prediction of tensile strength of discontinuous carbon fiber/polypropylene composite with fiber orientation distribution. *Composites Part A: Applied Science and Manufacturing*, 43(10):1791–1799, 2012.

[13] H. Fukuda and T Chou. A probabilistic theory of the strength of short-fibre composites with variable fibre length and orientation. *Journal of Materials Science*, 17:1003–1011, 1982.

[14] A. Kelly and W.R. Tyson. Tensile properties of fibre-reinforced metals: Copper/tungsten and copper/molybdenum. *Journal of the Mechanics and Physics of Solids*, 13:329–350, 1965.

[15] S. Pimenta and P. Robinson. An analytical shear–lag model for brick–and–mortar composites considering non-linear matrix response and failure. *Composites Science and Technology*, 104:111–124, 2014.

[16] P. Feraboli and M. Ciccu. AMTAS: Certificate of discontinuous composite material forms for aircraft structures. Seattle, May 2010. AMTAS Fall meeting.

[17] T. Y. Kam, H. F. Sher, T. N. Chao, and R. R. Chang. Predictions of deflection and first-ply failure load of thin laminated composite plates via the finite element approach. *International Journal of Solids and Structures*, 33(3):375–398, 1996.

[18] H. T. Hahn and S. W. Tsai. On the behavior of composite laminates after initial failure. *Journal of Composite Materials*, (8):288–305, 1974.

[19] S. W. Tsai and E. M. Wu. A general theory of strength for anisotropic materials. *Journal of Composite Materials*, 5:58–80, 1971.

[20] V. D. Azzi and S. W. Tsai. Anisotropic strength of composites. *Experimental Mechanics*, 5(9):283–288, 1965.

[21] Z. Hashin and B. W. Rosen. The elastic moduli of fiber-reinforced materials. *Journal of Applied Mechanics*, 31:223–232, 1964.

[22] S. Pinho, R. Darvizeh, P. Robinson, C. Schuecker, and P. Camanho. Material and structural response of polymer-matrix fibre-reinforced composites. *Journal of Composite Materials*, 46:2313–2341, 2012.

[23] S. S. Kaddour and M. J. Hinton. Maturity of 3D failure criteria for fibre-reinforced composites: Comparison between theories and experiments: Part B of WWFE-II. *Journal of Composite Materials*, 47:925–966, 2013.

[24] J. Henry and S. Pimenta. Semi-analytical simulation of aligned discontinuous composites. *Composites Science and Technology*, 144:230–244, 2017.

[25] P. Feraboli, E. Peitso, T. Cleveland, and P. B. Stickler. Modulus measurement for prepreg-based discontinuous carbon fiber/epoxy systems. *Journal of Composite Materials*, 43(19):1947–1965, 2009.

[26] P. Feraboli, T. Cleveland, M. Ciccu, P. B. Stickler, and L. de Oto. Defect and damage analysis of advanced discontinuous carbon fiber/epoxy composite materials. *Composites: Part A - Applied Science and Manufacturing*, 41(7):888–901, 2010.

[27] M. Selezneva, S. Roy, L. Lessard, and A. Yousefpour. Analytical model for prediction of strength and fracture paths characteristic to randomly oriented strand (ROS) composites. *Composites: Part B - Engineering*, 96(2016):103–111, 2016.

[28] M. Selezneva, S. Roy, , S. Meldrum, L. Lessard, and A. Yousefpour. Modelling of mechanical properties of randomly oriented strand thermoplastic composites. *Journal of Composite Materials*, 51(6):831–845, 2017.

[29] L. T. Harper, C. C. Qian, R. Luchoo, and N. A. Warrior. 3d geometric modelling of discontinuous fibre composites using a force-directed algorithm. *Journal of Composite Materials*, 0(0):1–18, 2016.

[30] S. Pimenta and S. T. Pinho. Hierarchical scaling law for the strength of composite fibre bundles. *Journal of the Mechanics and Physics of Solids*, 61(2013):1337–1356, 2013.

[31] E. J. Barbero, F. A. Cosso, R. Roman, and T. L. Weadon. Determination of material parameters for abaqus progressive damage analysis of e-glass epoxy laminates. *Composites part B: Engineering*, 46(2013):211–220, 2013.

[32] A. Matzenmiller, J. Lubliner, and R.L. Taylor. A constitutive model for anisotropic damage in fiber-composites. *Mechanics of Materials*, 20(1995):125–152, 1995.

[33] P. P. Camanho, A. Arteiro, A. R. Melro, G. Catalanotti, and M. Vogler. Three-dimensional invariant-based failure criteria for fibre-reinforced composites. *International Journal of Solids*

       and Structures, 55(2015):92–107, 2015.

[34] C. A. Felippa and E. Oñate. Stress, strain and energy splittings for anisotropic elastic solids under volumetric constraints. *Computers and Structures*, 81:1343–1357, 2003.

[35] HexMC M77 Moulding Concept Product Data. `http://www.hexcel.com/Resources/DataSheets/Molding-Data-Sheets/HexMC_C_2000_M77.pdf`, Oct 2014. Accessed: 2016-01-30.

[36] HexPly M77 Product Data. `http://www.hexcel.com/Resources/DataSheets/Prepreg-Data-Sheets/M77_eu.pdf`, Mar 2014. Accessed: 2016-01-30.

[37] MATLAB. *version 7.10.0 (R2016b)*. The MathWorks Inc., Natick, Massachusetts, 2016.

[38] S. Y. Fu and B. Lauke. Effects of fiber length and fiber orientation distributions on the tensile strength of short-fiber-reinforced polymers. *Composites Science and Technology*, 56(2):1179–1190, 1996.

[39] Y. Wan, T. Ohori, and J. Takahashi. Mechanical properties and modeling of discontinuous carbon fiber reinforced thermoplastics. 20th International Conference on Composite Materials; Copenhagen, Denmark, 19-24 July 2015.

[40] L. T. Harper, T. A. Turner, N. A. Warrior, and C. D. Rudd. Characterisation of random carbon fibre composites from a directed fibre preforming process: The effect of tow filamentisation. *Composites: Part A - Applied Science and Manufacturing*, 38(2007):755–770, 2007.
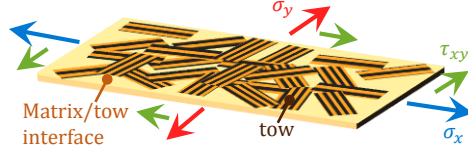
Figure 1: Tow-based discontinuous composite under a plane-stress state.
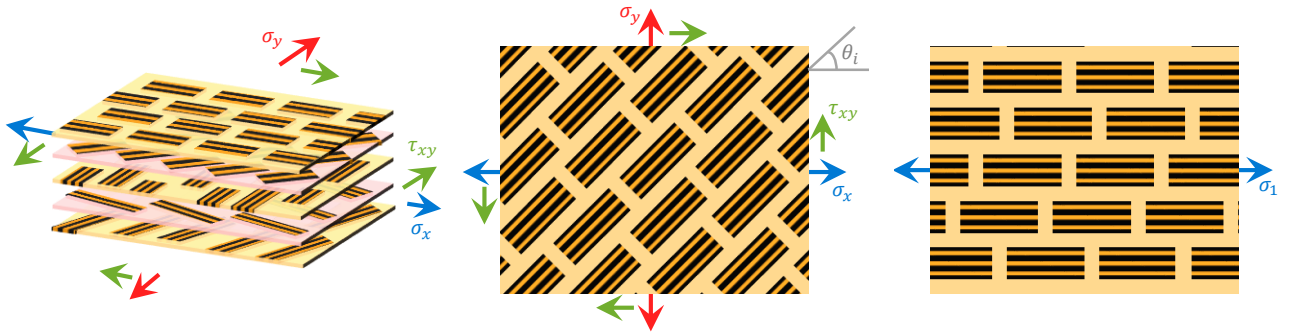
(a) Equivalent laminate.

(b) UD discontinuous ply at θ_i orientation.

(c) UD discontinuous ply under uni-axial tension.

Figure 2: Multi-scale architecture of TBDC assumed for modelling.

Table 1: Specification of the microstructure of the TBDCs analysed [35] .

Material	l_t (mm)	w_t (mm)	t_t (mm)	$V_{\mathrm{f,TBDC}}$ (%)
HexMC-M77 [35]	50.0	8.0	0.164 (default) 0.285	59.3 (default) 57.6

Table 2: UD material properties used as model inputs. The moduli are shown in GPa, strengths are in MPa, toughness is in kJ/m^2, and volume fraction in %.

Material	$E_{1,\mathrm{UD}}$	E_2	G_{12}	ν_{12}	$X_{\mathrm{UD}}^{\mathrm{T}}$	Y^{T}	Y^{C}	S	$\mathcal{G}_{\mathrm{IIc}}$	$V_{\mathrm{f,UD}}$
HexPly-M77 [36]	116‡	9.0†	5.6†	0.34†	1132‡	73†	200†	78.0⋆	0.80†	51.3⋆

‡ Values taken from uni-axial tensile tests on HexPly-M77; ⋆ Values taken from data-sheet [36]; † Educated guesses based on the literature [23]

Table 3: Numerical parameters used as model inputs.

Number of overlap lengths	Number of overlap thicknesses	Number of tows in a RVE	Number of stresses on τ_{12} and σ_2 axes in ITS criterion	Number of plies in the equivalent laminate
N_{lo}	N_{to}	N_{RVE}	N_{p}	N_{ply}
25	25 for RC, 1 for EL	900	100	36

25
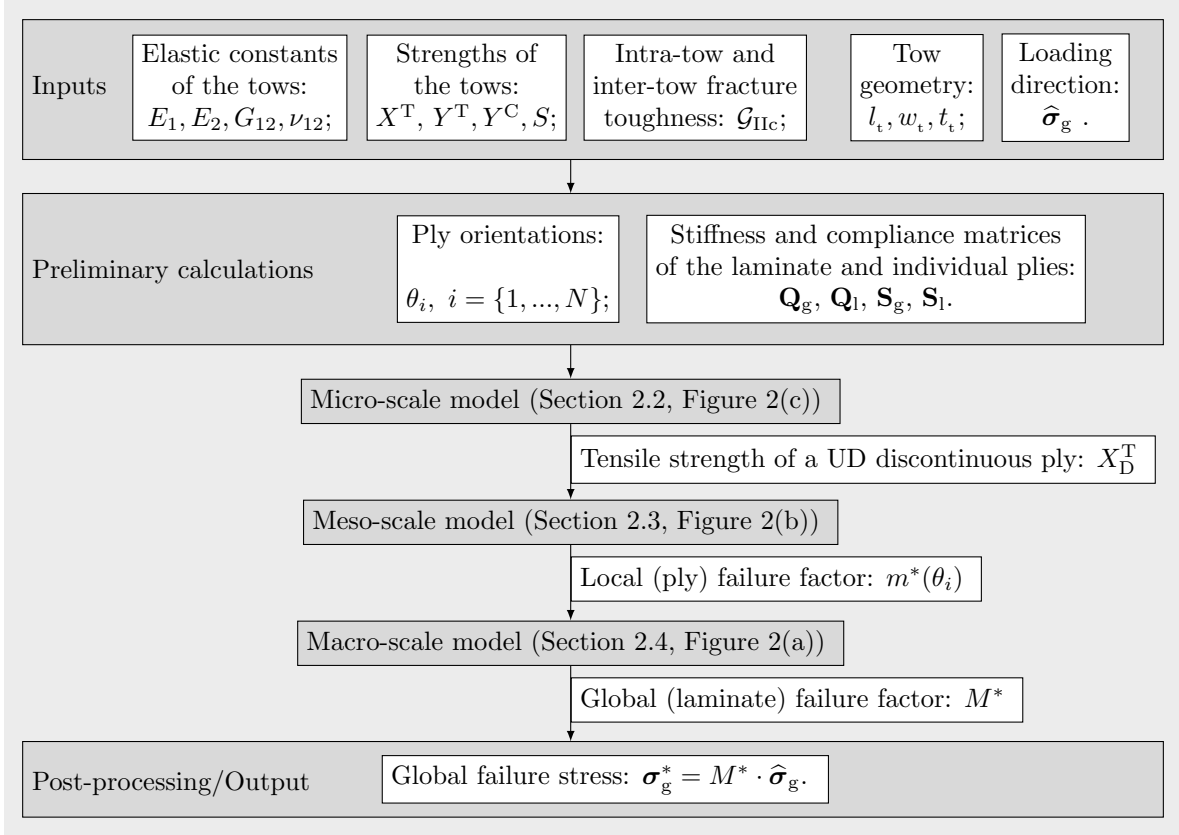
Figure 3: Flow-chart of the main calculations of the model.
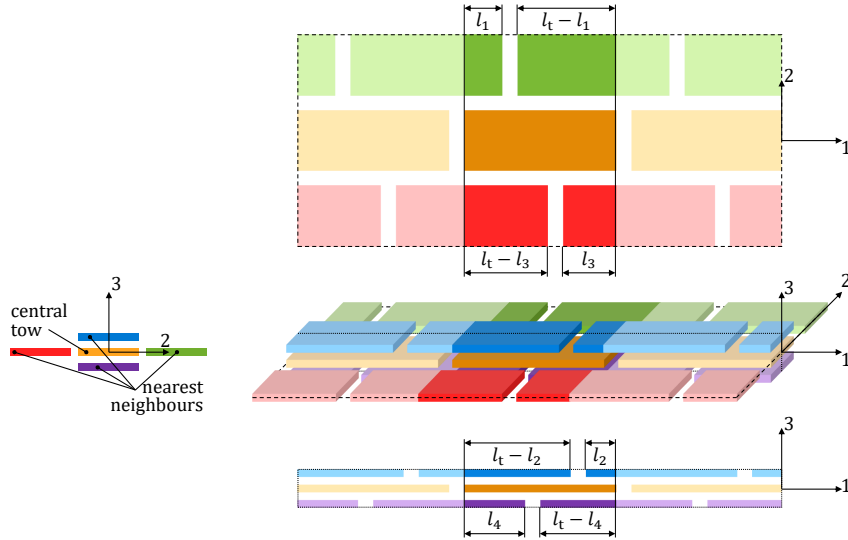
Figure 4: Micro-scale model with randomly-located tow ends. The central image shows a 3D representation of the *interactions* between tow (shown in orange) and its four nearest neighbours (one behind (in green), one above (in blue), one in front (in red), and one below (in purple). The image on the left shows the cross-section of the tow and its four nearest neighbours. The images at the top and bottom show 1D representations of the interactions between the central tow and its four nearest neighbours; the lengths indicated correspond to the two *overlap* lengths per *interaction*.
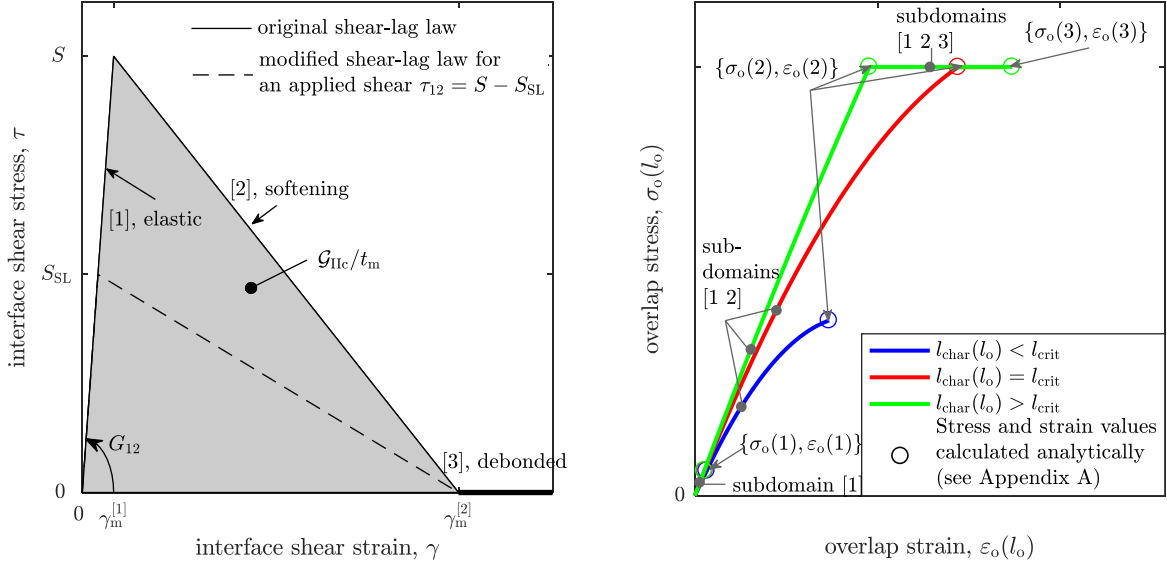
(a) Bi-linear shear stress-strain law assumed for the tow interface, composed by 3 subdomains: elastic [1], softening [2], and fully-debonded [3].

(b) Stress-strain response of several overlaps of different lengths l_{o}. The characteristic length is calculated as $l_{\mathrm{char}}(l_{\mathrm{o}}) = l_{\mathrm{o}}/2$, and the critical length l_{crit} is defined in Appendix A. The subdomains of the tow interface active in each overlap at the different applied stresses are shown in between square brackets.

Figure 5: Non-linear shear-lag model used to predict the stress-strain curve of tow overlaps.
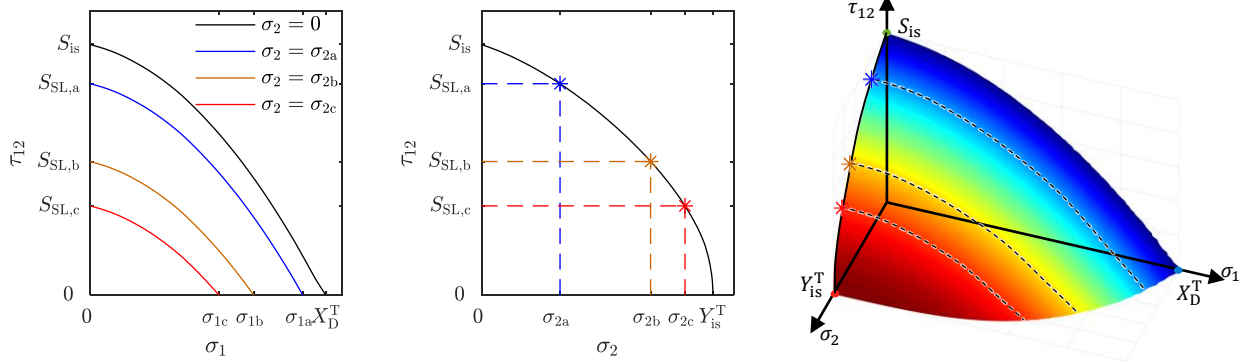
(a) Longitudinal/shear failure envelopes for different values of applied transverse tension σ_2.

(b) Transverse-shear failure envelope (assuming $\sigma_1 = 0$) from LaRC05.

(c) Failure surface of a $0°$ UD discontinuous ply obtained with the ITS criterion.

Figure 6: Failure envelopes calculated through the interactive tension-shear criterion (N_{to}=25). Taking an applied transverse stress $\sigma_2 = \sigma_{2a}$ in Figure (b), the maximum shear stress that can be sustained by the ply will be $S_{\mathrm{SL,a}}$ (calculated from the LaRC05 criterion in Eq. 6); for any applied shear stress $\tau_{12} \in [0, S_{\mathrm{SL,a}}]$ superposed with σ_{2a}, the maximum longitudinal stress can be calculated through the shear-lag model, considering the available shear stress for shear-lag $S_{\mathrm{SL}} = S_{\mathrm{SL,a}} - \tau_{12}$; this gives the curve labelled as $\sigma_2 = \sigma_{2a}$ in Figure (a).
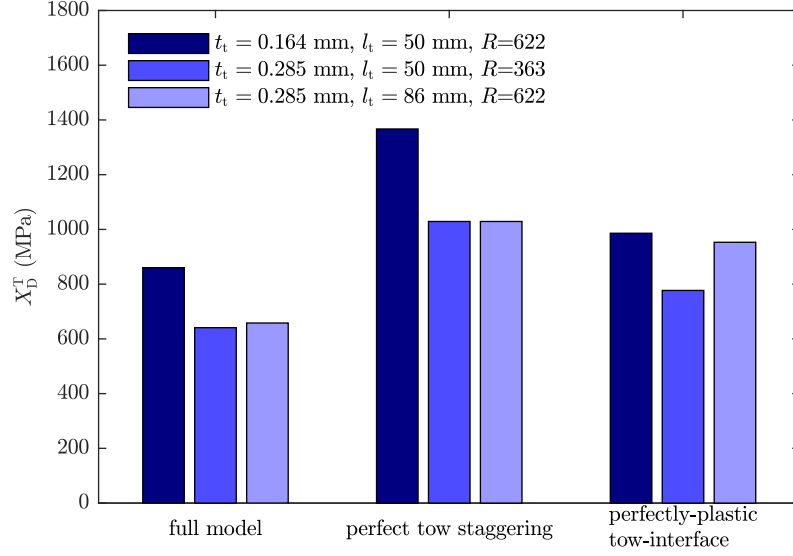
Figure 7: Uni-axial tensile strength of a UD discontinuous ply with different tow geometries (N_{to}=25), predicted by the micro-scale model as presented in Section 2.2 ("full-model"), or by two simplified versions of the micro-scale model ("perfect tow staggering" and "perfectly-plastic interface").
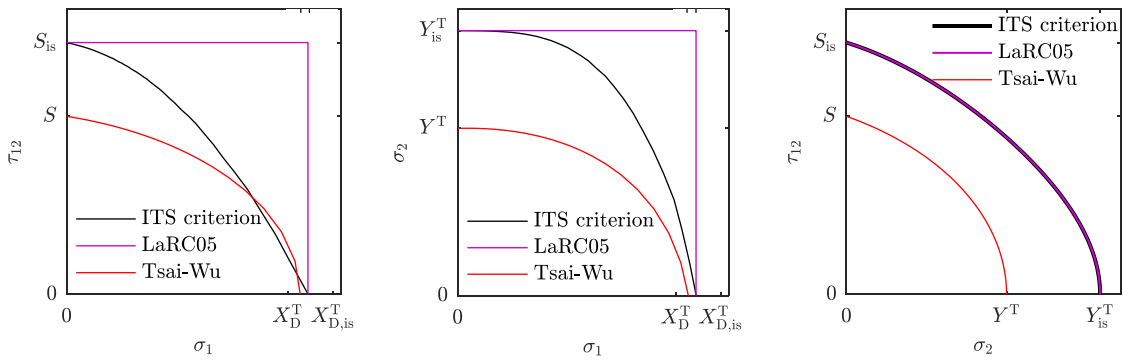
(a) Longitudinal vs. shear stress. (b) Longitudinal vs. transverse stress. (c) Transverse vs. shear stress.

Figure 8: Failure envelopes of a UD discontinuous ply obtained with the ITS criterion, compared with LaRC05 [22] and Tsai-Wu's [20] failure criteria (N_{to}=25).
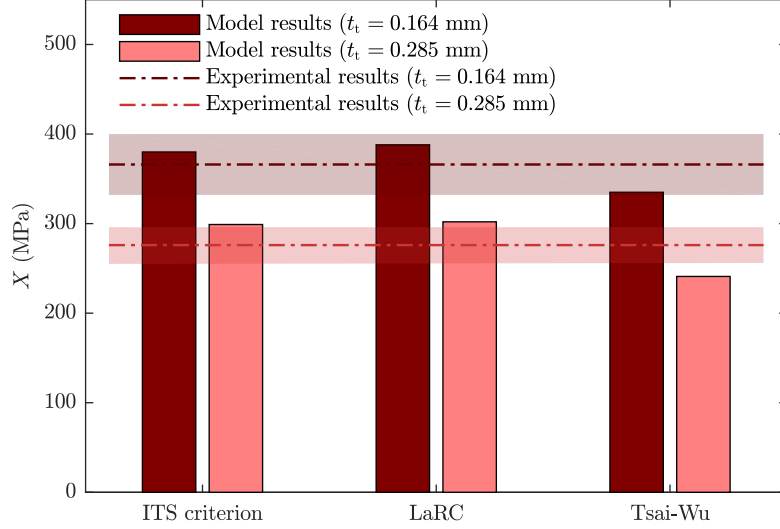
Figure 9: Uniaxial tensile strength of TBDCs with two different tow thicknesses obtained with the ITS criterion (N_{to}=1), compared with LaRC05 [22] and Tsai-Wu's [20] failure criteria, and compared against experimental results for equivalent laminates (shaded region represents the standard deviation measured in the experiments) [7].

Table A.4: Derivation of the transition points in the stress-strain relation for a tow overlap, using the bi-linear shear-lag model.

Transition of active interface subdomains	Analytical stress and strain values	
$[1] \rightarrow [1\ 2]$	$\sigma_{\text{o}}(1) = \dfrac{2}{\lambda^{[1]} \cdot t_{\text{o}}} S \cdot \tanh(\lambda^{[1]} \cdot l_{\text{o}}); \quad \varepsilon_{\text{o}}(1) = \dfrac{\sigma_{\text{o}}(1)}{E_1} + \dfrac{t_{\text{m}} \cdot \gamma_{\text{m}}^{[1]}}{2l_{\text{o}}};$	
$[1\ 2] \rightarrow [2]$ $(l_{\text{o}} \leq l_{\text{crit}})$	$\sigma_{\text{o}}(2) = \sqrt{\dfrac{E_1 \cdot \mathcal{G}_{\text{IIc}}}{t_{\text{o}}}};$	
or $[1\ 2] \rightarrow [1\ 2\ 3]$ $(l_{\text{o}} > l_{\text{crit}})$	$\varepsilon_{\text{o}}(2) = \begin{cases} \dfrac{\sigma_{\text{o}}(2)}{E_1} + \dfrac{t_{\text{m}}}{2l_{\text{o}}}\left(\gamma_{\text{m}}^{[1]} + \dfrac{S}{G^{[2]}}(1 - \cos(\lambda^{[2]} \cdot l_{\text{o}}))\right) & l_{\text{o}} \leq l_{\text{crit}}; \\[3ex] \dfrac{\sigma_{\text{o}}(2)}{E_1} + \dfrac{t_{\text{m}} \cdot \gamma_{\text{m}}^{[2]}}{2l_{\text{o}}} & l_{\text{o}} > l_{\text{crit}}; \end{cases}$	
$[1\ 2\ 3] \rightarrow [2\ 3]$ $(l_{\text{char}} > l_{\text{crit}})$	$\sigma_{\text{o}}(3) = \sqrt{\dfrac{E_1 \cdot \mathcal{G}_{\text{IIc}}}{t_{\text{o}}}};$ $\varepsilon_{\text{o}}(3) = \dfrac{\sigma_{\text{o}}(3)}{E_1} + \dfrac{t_{\text{m}}}{2l_{\text{o}}}\left(\gamma_{\text{m}}^{[2]} + \dfrac{2\sigma_{\text{o}}(2)}{E_1 \cdot t_{\text{m}}}(l_{\text{o}} - \dfrac{\pi}{2\lambda^{[2]}})\right)$	$l_{\text{o}} > l_{\text{crit}}.$

where $\lambda^{[i]} = \sqrt{\dfrac{2|G^{[i]}|}{t_{\text{o}} \cdot t_{\text{m}} \cdot E_1}}$, and $G^{[1]} = G_{12}, \ G^{[2]} = -\dfrac{S}{\gamma_{\text{m}}^{[2]} - \gamma_{\text{m}}^{[1]}}; \ \gamma_{\text{m}}^{[1]} = \dfrac{S}{G_{12}}, \ \gamma_{\text{m}}^{[2]} = \dfrac{2\mathcal{G}_{\text{IIc}}}{S \cdot t_{\text{m}}}.$
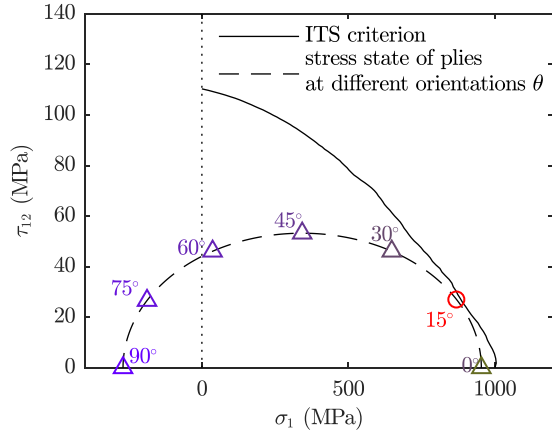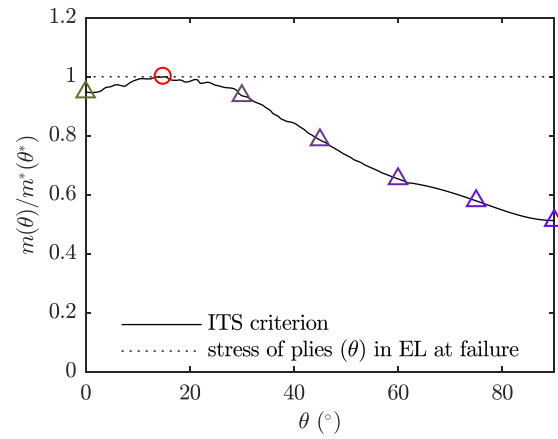
(a) Longitudinal-shear stresses.
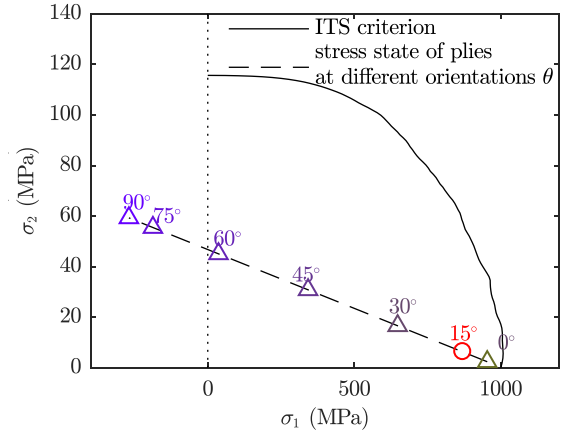
(b) Longitudinal-transverse stresses.
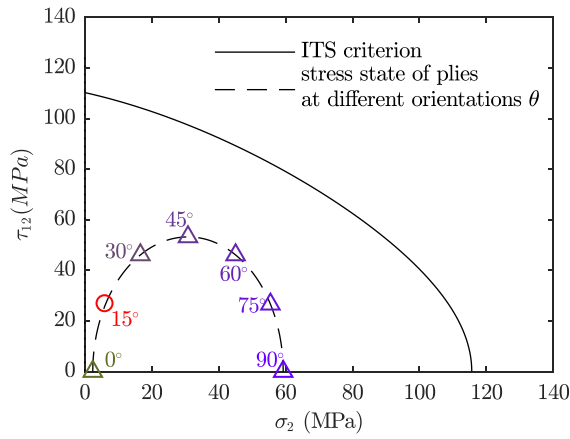
(c) Transverse-shear stresses.

(d) Ratio of stress magnitude in each ply to the failed ply ($12°$ ply).

Figure 10: Stress distribution in the plies of a quasi-isotropic EL (with $N_{\mathrm{ply}} = 180$ plies, $N_{\mathrm{to}}=25$, equally spaced by $\Delta\theta = 1°$) under uni-axial tension, at first ply failure (which occurs for the $14°$ ply).
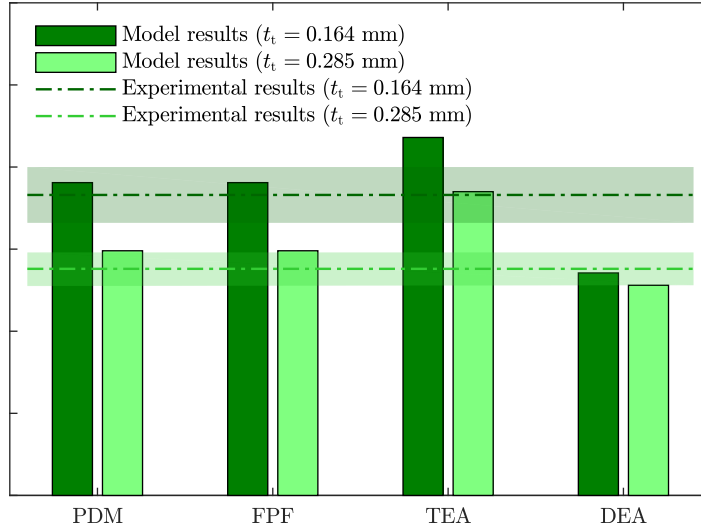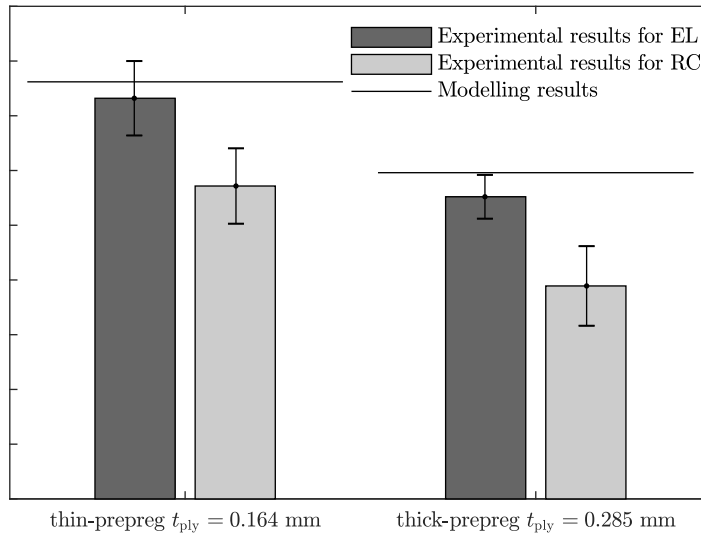
Figure 11: Strength predicted by the ply-discount method (PDM), first-ply-failure (FPF) method, total energy approach (TEA), and decomposed energy approach (DEA), compared against experimental data for equivalent laminates (shaded region represents the standard deviation measured in the experiments, $N_{to}=1$) [7].

Figure 12: Strength predicted by the model for a QI TBDC under uni-axial tension ($N_{to}=1$), compared to the experimental data for QI equivalent laminate (EL) and randomly-oriented TBDC (RC) [7].
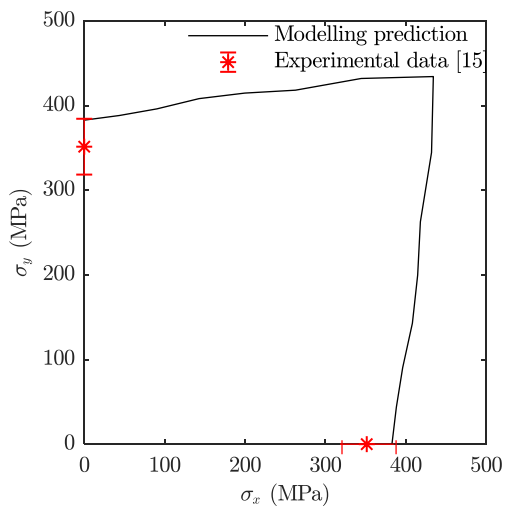
(a) Bi-axial failure envelope.
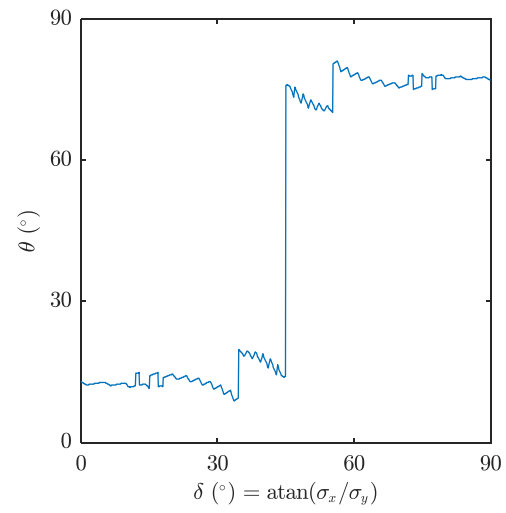
(b) Orientation of the first failed ply for different loading ratios $\delta = \arctan(\sigma_x/\sigma_y)$.

Figure 13: Model predictions for TBDCs under biaxial (applied σ_x and σ_y, with $\tau_{xy} = 0$) loading (N_{to}=1).
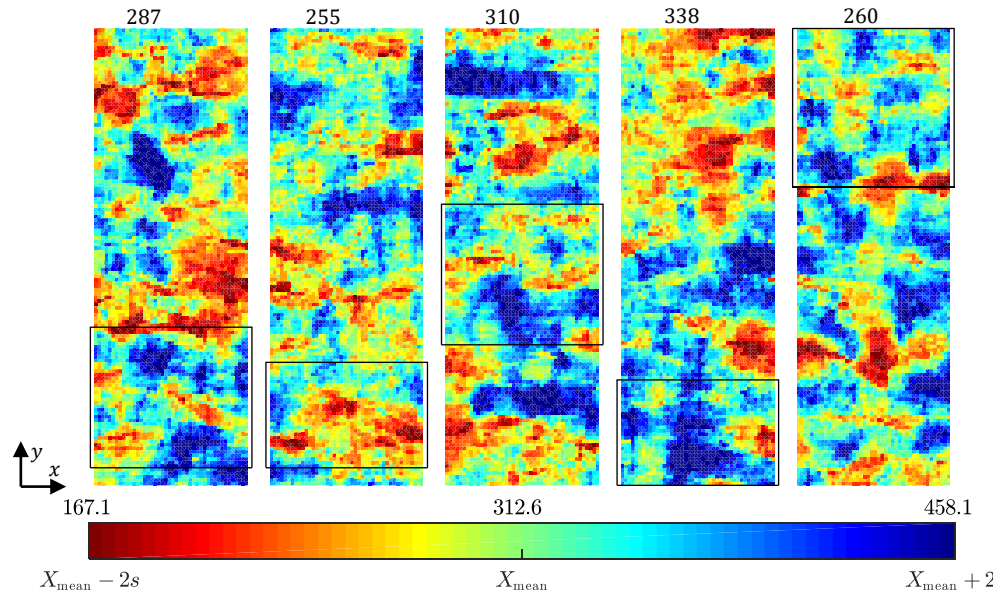
(a) Strength map calculated for thin-prepreg (0.164 mm) TBDC specimens, considering variability in local tow orientation only.
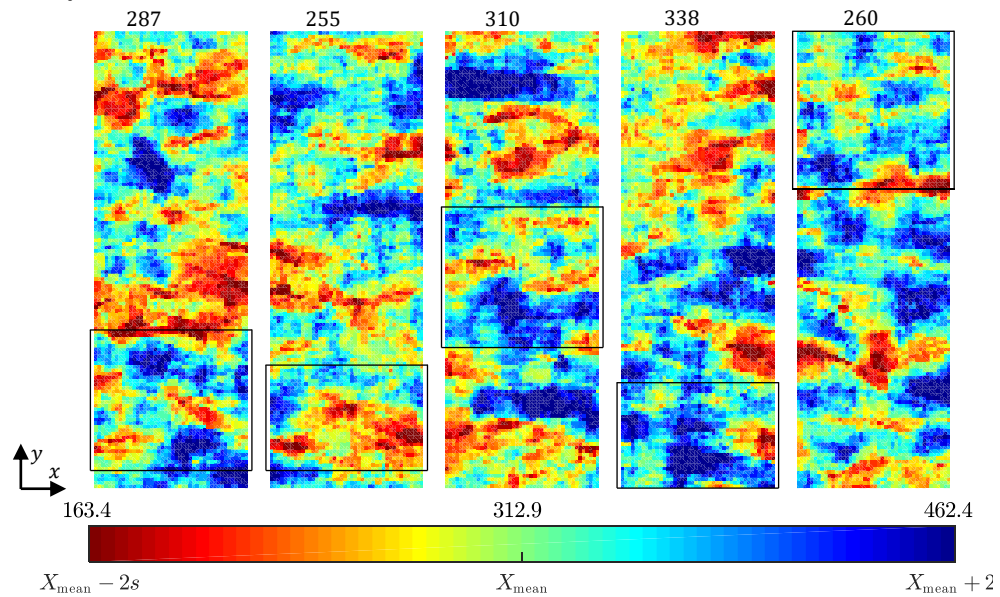
(b) Strength map calculated for thin-prepreg (0.164 mm) TBDC specimens, considering variability in both local tow orientation and local fibre volume fraction.
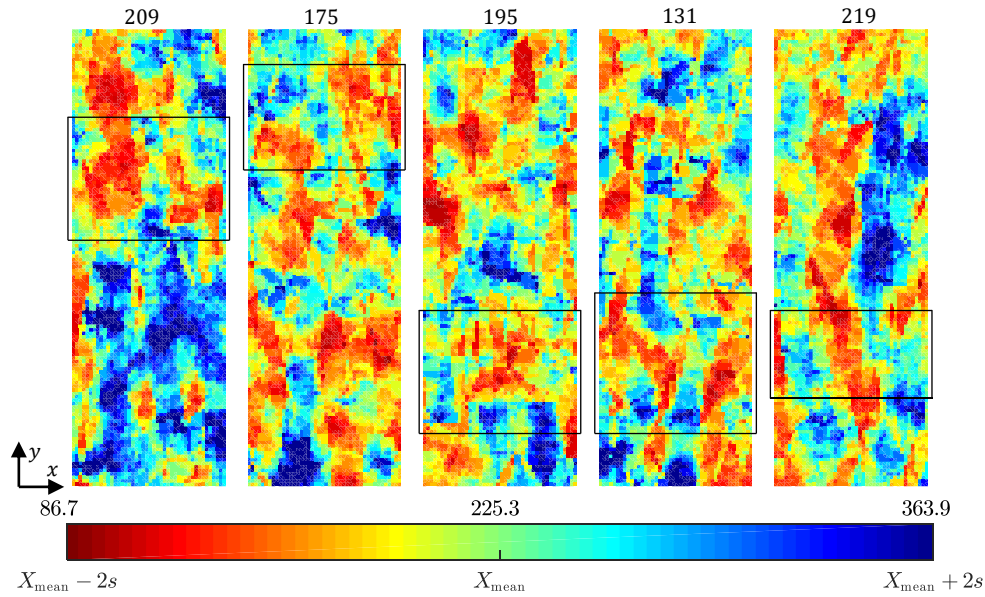
(c) Strength map calculated for thick-prepreg (0.285 mm) TBDC specimens, considering variability in local tow orientation only.
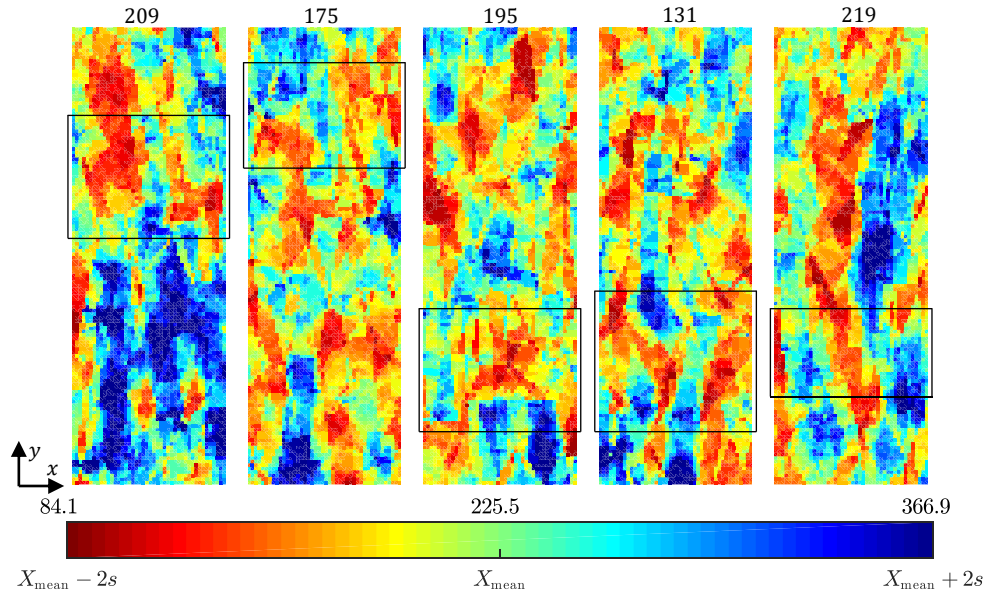

(d) Strength map calculated for thick-prepreg (0.285 mm) TBDC specimens, considering variability in both local tow orientation and local fibre volume fraction.

Figure 14: Local strength (in MPa) maps in the gauge section of QI randomly-oriented TBDC specimens loaded under uni-axial tension [7], calculated by the present model and from the local microstructure of the specimens. The black boxes represent the failure regions observed experimentally in the specimens, X_{mean} represents the average strength/strength of the QI EL, and s represents one standard deviation of the local strength distribution. The strength experimentally measured for each specimen has been added at the top of each contour (N_{to}=25).
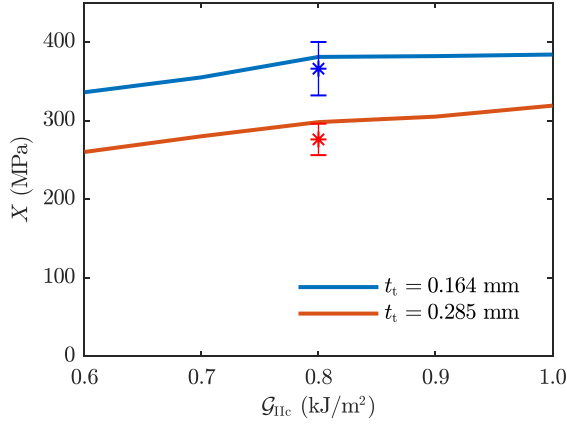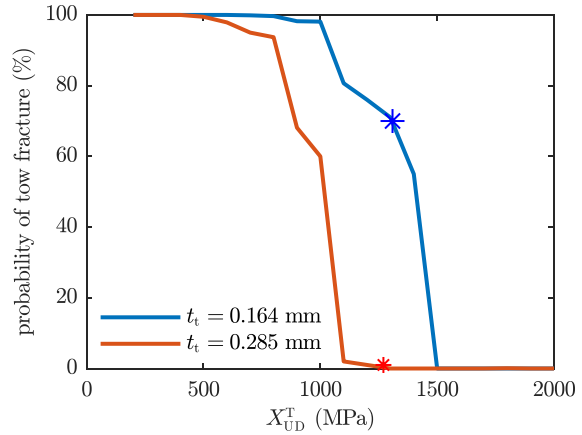
(a) Effect of prepreg mode-II fracture toughness on the strength of TBDCs.
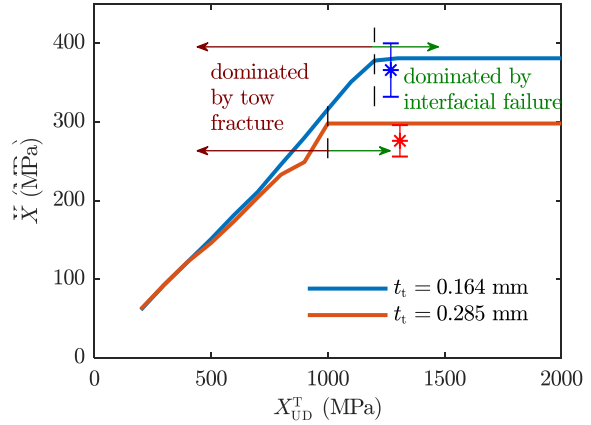
(b) Effect of prepreg longitudinal strength on the strength of TBDCs.
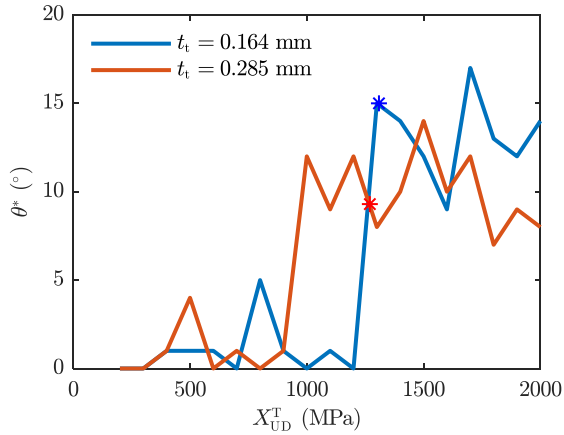
(c) Effect of prepreg longitudinal strength on the orientation of the first failed ply.

(d) Effect of prepreg longitudinal strength on the percentage of tow fracture in a $0°$ ply (N_{to}=25).

Figure 15: Effect of prepreg properties on the strength and failure mode of TBDCs (N_{to}=1).